

# Towards the Habitable Worlds Observatory: 1D CNN Retrieval of Reflection Spectra from Evolving Earth Analogs

Sarah G. A. Barbosa,<sup>1</sup>★ Raissa Estrela,<sup>2</sup> Paulo C. F. da Silva Filho<sup>1</sup> and Daniel B. de Freitas<sup>1</sup>

<sup>1</sup>*Departamento de Física, Universidade Federal do Ceará, Campus do Pici, 6030, Fortaleza, CE 60455-900, Brazil*

<sup>2</sup>*Jet Propulsion Laboratory, California Institute of Technology, 4800 Oak Grove Drive, Pasadena, CA 91109, USA*

Accepted XXX. Received YYY; in original form ZZZ

## ABSTRACT

Upcoming direct-imaging missions like the Habitable Worlds Observatory (HWO) aim to characterize dozens of Earth-like exoplanets by capturing their reflected-light spectra. However, traditional atmospheric retrieval frameworks are too computationally intensive to explore the high-dimensional parameter spaces such missions will generate. Here, we demonstrate that a one-dimensional convolutional neural network (1D CNN), trained on over one million synthetic, noise-injected spectra simulating Archean, Proterozoic, and Modern Earth analogs (as observed by LUVOIR-B from 0.2 to 2.0  $\mu\text{m}$  and by HabEx/SS from 0.2 to 1.8  $\mu\text{m}$ ), can rapidly retrieve key planetary parameters. Our model simultaneously infers six molecular abundances (including biosignatures  $\text{O}_2$  and  $\text{O}_3$ ) along with radius, gravity, surface pressure, and temperature. Inference on unseen test data is performed via Monte Carlo Dropout, enabling uncertainty estimation across thousands of realizations within seconds. The network performs best where spectral features are prominent, accurately recovering  $\text{CH}_4$  and  $\text{CO}_2$  in Archean atmospheres and  $\text{O}_2$  and  $\text{O}_3$  in Modern cases, while avoiding false positives and outputting near-zero abundances in scenarios of true absence such as Archean  $\text{O}_2$  and  $\text{O}_3$ . Interpretation via Integrated Gradients confirms that the model bases its predictions on physically meaningful features, including the Fraunhofer A band for  $\text{O}_2$ , and the Hartley–Huggins band for  $\text{O}_3$ . Credibility curve analysis indicates that  $\text{O}_3$  remains retrievable across a wide range of stellar types and distances, while  $\text{O}_2$  is detectable out to 12 pc around F-, G- type stars. These results elevate the CNN from proof of concept to a mission-ready retrieval engine, capable of processing direct-imaging spectra with HWO on an operational cadence.

**Key words:** planets and satellites: atmospheres – exoplanets – software: machine learning

## 1 INTRODUCTION

Since the discovery of the first exoplanet orbiting a Sun-like star in 1995 (Mayor & Queloz 1995), over 6,000 exoplanets have been confirmed<sup>1</sup>. These objects span a wide range of sizes, orbital configurations, and compositions, revealing a diversity that challenges classical paradigms of planetary formation (Morbidelli & Raymond 2016). Most known exoplanetary systems differ dramatically from our own Solar System, featuring “exotic” worlds such as hot Jupiters and super-Earths (Charbonneau et al. 2009; Haghighipour 2013; Dawson & Johnson 2018; Fortney et al. 2021).

As detection rates surge, atmospheric characterization emerges as the next step in exoplanet research (Charbonneau et al. 2002, 2005; Gibson et al. 2010; Brogi et al. 2012; Deming & Seager 2017; Estrela et al. 2022). This is especially critical for Earth-like exoplanets which are considered the “holy grail” of exoplanetary science (Howard et al. 2013). Yet, characterizing these planets remains difficult due to faint atmospheric signals obscured by stellar brightness. Consequently, most atmospheric studies focus on giant planets using transmission spectroscopy to probe upper atmospheric layers during transits (e.g.,

Kreidberg et al. 2014; Tsiaras et al. 2019; Robinson et al. 2017; JWST Transiting Exoplanet Community Early Release Science Team et al. 2023). This method has limitations: it requires favorable near-edge-on orbital geometries (statistically rare) and is most effective for close-in planets, given that distant exoplanets often have prohibitively long orbital periods.

Direct imaging offers a complementary method by isolating planetary signals, enabling direct atmospheric profiling through reflection spectroscopy. Advances in adaptive optics and coronagraph technology promise the necessary contrast ratios to characterize rocky planets directly (Damiano & Hu 2022; Damiano et al. 2023; Robinson & Salvador 2023; Currie et al. 2023). A key upcoming mission in these efforts is NASA’s *Habitable Worlds Observatory* (HWO), conceived as a future flagship mission based on concepts from the Habitable Exoplanet Observatory (HabEx) and the Large Ultraviolet/Optical/InfraRed Surveyor (LUVOIR) (The LUVOIR Team 2019; Gaudi et al. 2020; Coston et al. 2024). Following recommendations from the Decadal Survey on Astronomy and Astrophysics 2020 (Astro2020) (National Academies of Sciences and Medicine, Engineering 2021), the HWO aims to detect and characterize approximately 25 potentially habitable exoplanets by capturing spectra across ultraviolet (UV), visible (VIS), and near-infrared (NIR) wavelengths. This will enable detection of biosignature gases such as  $\text{O}_2$  and  $\text{O}_3$ , key indicators of potential habitability (Damiano et al. 2023).

★ E-mail: sarah@fisica.ufc.br

<sup>1</sup> For the latest count, see the NASA Exoplanet Archive: <https://exoplanetarchive.ipac.caltech.edu/>.

When considering potentially habitable worlds, Earth serves as the primary natural laboratory (e.g., Arney et al. 2016; Rugheimer & Kaltenegger 2018; Kofman et al. 2024). Earth-like planets are considered to exhibit atmospheres dominated by  $N_2$  (a recycled, dissolved gas),  $CO_2$  (a non-condensable greenhouse gas), and  $H_2O$  (a condensable greenhouse gas) (Kopparapu et al. 2013; Schwieterman et al. 2018). However, this description reflects only Earth’s present-day state. Over geological timescales, Earth’s atmospheric composition has undergone dramatic changes (Lyons et al. 2014). While hydrogen-rich atmospheres may exist elsewhere, Earth’s evolution provides an empirical support for understanding how inhospitable planets may develop life-sustaining conditions.

For example, during the Archean eon (4.0–2.5 Gyr ago), intense volcanic activity and the Late Heavy Bombardment reshaped Earth’s surface, while the atmosphere was dominated by  $N_2$ ,  $CH_4$ , and  $CO_2$  with negligible  $O_2$  (Catling & Zahnle 2020). The subsequent Proterozoic eon (2.5 Gyr–500 Myr ago) saw the Great Oxidation Event (GOE), driven by photosynthetic microorganisms, which dramatically increased atmospheric  $O_2$  levels (Planavsky et al. 2014). Although Proterozoic  $O_2$  and  $O_3$  levels were insufficient to produce strong VIS band absorption features, they significantly influenced the UV regime (Damiano et al. 2023).

The Phanerozoic eon (last 500 Myr) includes the Cambrian explosion, a pivotal diversification of complex life (Marshall 2006; Catling & Kasting 2017). Despite its relatively short duration, the Phanerozoic is the most extensively documented period of Earth’s history due to well-preserved geological records and abundant fossil evidence. During this eon, Earth’s atmosphere stabilized into its modern composition, dominated by  $N_2$  and  $O_2$ .

These geological epochs serve as templates for interpreting the diversity of atmospheric conditions on rocky exoplanets. A key challenge, however, lies in reliably extracting meaningful atmospheric parameters from observational data (Changeat & Yip 2023). Current retrieval methods typically fall into two categories: (1) forward models, integrating detailed atmospheric physics and chemistry to generate synthetic spectra (e.g., Goyal et al. 2018; Zhang et al. 2019), and (2) retrieval methods, which statistically infer atmospheric parameters directly from observed spectra (e.g., Madhusudhan & Seager 2009; Waldmann et al. 2015; Lavie et al. 2017). Both methods, however, face computational limitations as complexity and fidelity increase, often necessitating simplifications that reduce precision.

Machine learning (ML), particularly deep learning (DL), offers a promising solution to these challenges. DL techniques can reduce computational costs, capture non-linear correlations, and scale efficiently with large datasets (Nixon & Madhusudhan 2020; Ardévol Martínez et al. 2022; Yip et al. 2024). These methods have been successfully applied in diverse fields, including image classification (Zhang et al. 2017; Li et al. 2019; Yadav et al. 2024), time-series analysis (Choi et al. 2021; Pathmaperuma et al. 2022; Zamanzadeh Darban et al. 2022), and exoplanet transit detection (Shallue & Vanderburg 2018; Valizadegan et al. 2022; Malik et al. 2022). For atmospheric retrieval, pioneering work by Waldmann (2016) introduced RobERT, a deep-belief neural network for classifying exoplanet spectra. Subsequent advances include ExoGAN (Zingales & Waldmann 2018) for retrieval parameter prediction and Neural Spline Flows for posterior estimation (Aubin et al. 2023). More recently, Zorzan et al. (2025) developed the INARA, the first ML retrieval model tailored to rocky exoplanets, using a synthetic dataset of 3 million spectra generated with NASA’s Planetary Spectrum Generator (PSG).

To support the science goals of future direct imaging missions such as HWO, we present a one-dimensional Convolutional Neural Network (1D-CNN) trained on 1,086,914 synthetic reflection spectra of

Earth-like planets spanning Archean, Proterozoic, and Modern atmospheric compositions. The dataset was generated using PSG, which forward-modeled spectra as observed by LUVIR-B and HabEx/SS at low spectral resolution. Our model simultaneously retrieves six molecular mixing ratios ( $CH_4$ ,  $CO_2$ ,  $H_2O$ ,  $N_2$ ,  $O_2$ ,  $O_3$ ) and four planetary parameters (radius, gravity, surface temperature, and pressure). Unlike previous deep learning models (such as INARA, which was trained on noiseless spectra, or ExoGAN, which targets hot Jupiters) our approach introduces three novel elements: (1) inclusion of mission-specific noise consistent with LUVIR/HabEx design specifications, (2) training optimized for the detection of  $O_2$  and  $O_3$ , biosignatures critical for distinguishing abiotic from biological atmospheric evolution, and (3) interpretability via integrated gradients, highlighting the spectral features most responsible for each prediction.

The paper is structured as follows. The Section 2 details the methodology for generating synthetic reflection spectra and planetary configurations. The Section 3 describes CNN architecture, training, and evaluation. The Section 4 presents retrieval results, and the Section 5 discusses conclusions and implications.

## 2 TRAINING DATA GENERATION

The synthetic reflection spectra dataset was generated using NASA’s PSG<sup>2</sup> (Villanueva et al. 2018), a radiative transfer model that synthesizes planetary spectra by coupling atmospheric radiative transfer equations with high-resolution spectroscopic databases. For efficient large-scale data generation, we employed a locally hosted PSG instance running within a Docker container, following the implementation guidelines provided by Villanueva et al. (2022).

Each spectrum is defined by a configuration dictionary that specifies stellar, orbital, atmospheric, surface, and instrument parameters<sup>3</sup>. For every configuration PSG returns the reflectance spectra, transmittance profiles and instrument noise estimates. Building the training set involves two integrated steps: (1) Habitability screening: we first applied physical criteria that ensure long-term atmospheric retention and the potential for surface liquid water and (2) Sample realization: for each viable configuration, we drew gas mixing ratios consistent with Archean, Proterozoic, or Modern Earth analogs and assigned observational parameters corresponding to LUVIR-B or HabEx/SS exposure scenarios. The subsections that follow describe each component in detail.

### 2.1 Circumstellar habitable zone for FGK stars

A key driver in the search for exoplanets is the discovery of potentially habitable worlds. However, the concept of *habitability* is complex and influenced by several factors, including the characteristics of the host star, system dynamics, and the planet’s specific composition (Kane 2021). Our understanding of habitability is primarily based on the conditions that support life on Earth. These include a combination of favorable physico-chemical aspects: the presence of a highly versatile solvent (water), a suitable temperature range, an energy source, and essential biological elements (CHNOPS: Carbon, Hydrogen, Nitrogen, Oxygen, Phosphorus, Sulfur) (Owen 1980; Cockell et al. 2016).

The circumstellar habitable zone (CHZ), a theoretical region

<sup>2</sup> <https://psg.gsfc.nasa.gov>

<sup>3</sup> A full parameter reference is available at <https://psg.gsfc.nasa.gov/helpapi.php#parameters>.

around a star where rocky planets can sustain surface liquid water, serves as a foundational framework for this search (Kasting et al. 1993; Brack 1993; Kaltenegger 2017). Kopparapu et al. (2014) proposed a model to approximate CHZ boundaries for planets of  $0.1\text{--}5 M_{\oplus}$  around stars with  $2600\text{ K} \leq T_{\text{eff}} \leq 7200\text{ K}$ . In this model, the inner edge corresponds to a  $\text{H}_2\text{O}$  dominated atmosphere (runaway greenhouse), while the outer edge corresponds to a  $\text{CO}_2$  dominated atmosphere (maximum greenhouse), with  $\text{N}_2$  acting as a background gas. We adopt the *optimistic* CHZ, bounded by the Recent Venus ( $S_{\text{RV}}$ ) and Early Mars ( $S_{\text{EM}}$ ) limits. Both insolation boundaries are expressed as fourth-order polynomials in  $T_0 \equiv T_{\text{eff}} - 5780\text{ K}$ ,

$$S_{\text{EM}} = 0.32 + 5.547 \times 10^{-5} T_0 + 1.526 \times 10^{-9} T_0^2 - 2.874 \times 10^{-12} T_0^3 - 5.011 \times 10^{-16} T_0^4, \quad (1)$$

$$S_{\text{RV}} = 1.776 + 2.136 \times 10^{-4} T_0 + 2.533 \times 10^{-8} T_0^2 - 1.332 \times 10^{-11} T_0^3 - 3.097 \times 10^{-15} T_0^4. \quad (2)$$

To compute orbital distances inside this zone, we first draw stellar parameters (effective temperature ( $T_{\text{eff}}$ ) and radius ( $R_{\star}$ )) from the mean values for F, G, and K dwarfs tabulated by Mamajek (2019). These spectral types are favored because their long main-sequence lifetimes permit biological evolution, unlike the short-lived O-, B-, and A-type stars (Cuntz & Guinan 2016). Luminosity is then obtained via the Stefan–Boltzmann relation, and the CHZ bounds follow as,

$$d = \left( \frac{L_{\star}/L_{\odot}}{S} \right)^{1/2}, \quad (3)$$

where  $S$  takes  $S_{\text{RV}}$  for the inner edge and  $S_{\text{EM}}$  for the outer edge. The resulting distance interval defines the orbital-radius prior for our synthetic planet catalogue.

## 2.2 Criteria for sustaining atmosphere and habitability

Beyond the geometric limits of the CHZ, a rocky planet must satisfy additional conditions for surface liquid water to endure. Chief among them is the presence of an atmosphere, which regulates the planet’s radiative-convective energy budget by coupling stellar insolation to thermal emission and interior heat flow (Seager 2013; Keles et al. 2018).

We therefore consider three critical factors governing atmospheric retention under habitable conditions: (1) surface pressure ( $P_{\text{surf}}$ ), determined by the planet’s mass-radius (M-R) relation; (2) surface temperature ( $T_{\text{surf}}$ ), governed primarily by incident stellar flux and atmospheric opacity; and (3) the cosmic shoreline, an empirical boundary that links stellar irradiation and planetary gravity to the long-term retention or loss of volatile envelopes. The remainder of this subsection quantifies each of these parameter and defines the acceptance criteria applied.

### 2.2.1 Surface pressure

Direct measurements of exoplanetary surface pressure are not yet feasible, so we rely on first-order hydrostatic scaling coupled to empirical M–R relations. Observationally derived M–R trends are usually expressed as piece-wise power laws that track compositional regimes (e.g., Hatzes & Rauer 2015; Otegi et al. 2020). For terrestrial bodies, Chen & Kipping (2017) find

$$R_{\text{p}} \propto M_{\text{p}}^{0.279 \pm 0.009}, \quad (4)$$

a result corroborated by the more recent analysis of Müller et al. (2024) (differences confined to the third decimal for  $M_{\text{p}} \lesssim 4.4 M_{\oplus}$ ).

Assuming a simple, isothermal hydrostatic atmosphere (McIntyre et al. 2023), the surface pressure in Earth units obeys

$$\frac{P_{\text{surf}}}{P_{\oplus}} = \left( \frac{M_{\text{p}}}{M_{\oplus}} \right)^2 \left( \frac{R_{\oplus}}{R_{\text{p}}} \right)^4. \quad (5)$$

Substituting Equation 4 yields a radius-only form,

$$\frac{P_{\text{surf}}}{P_{\oplus}} = \left( \frac{R_{\text{p}}}{R_{\oplus}} \right)^{3.168 \pm 0.232}, \quad (6)$$

where  $P_{\oplus} = 1.014\text{ bar}$  is modern Earth’s surface pressure.

To maintain physical plausibility, we adopt the radius bounds proposed by McIntyre et al. (2023):  $R_{\text{p}} \in [0.3, 1.23] R_{\oplus}$ , spanning the range from the smallest confirmed rocky exoplanet around a main-sequence star (Barclay et al. 2013) up to the empirical transition between terrestrial and volatile-rich worlds (Chen & Kipping 2017). Within this interval Equation 6 yields surface pressures from  $\sim 0.1$  to  $\sim 2\text{ bar}$ .

### 2.2.2 Surface temperature

Surface temperature is also a key parameter for establishing the phase stability of liquid water. Although  $T_{\text{surf}}$  can in principle be obtained directly from sophisticated radiative-convective or general-circulation models (Way et al. 2017; Phillips et al. 2020), such treatments are far too computationally intensive. Instead, we adopt a semi-analytical approach that rescales the planet’s equilibrium temperature ( $T_{\text{eq}}$ ) by a simple greenhouse-effect factor.

The equilibrium temperature represents the black-body temperature of a planet in radiative balance with its host star (Seager 2010):

$$T_{\text{eq}} = \left[ \frac{(1 - A) I_{\star}}{4\sigma} \right]^{1/4}, \quad (7)$$

where  $A$  is the Bond albedo,  $\sigma$  is the Stefan–Boltzmann constant, and the stellar insolation relative to Earth is,

$$\frac{I_{\star}}{I_{\oplus}} = \frac{L_{\star}}{L_{\odot}} \left( \frac{a_{\oplus}}{a_{\text{p}}} \right)^2, \quad (8)$$

with  $a_{\text{p}}$  the planet’s semi-major axis. To convert  $T_{\text{eq}}$  to a surface value, we follow the idealized greenhouse prescription of Seager (2010),

$$T_{\text{surf}} = \left( \frac{2}{2 - \varepsilon} \right)^{1/4} T_{\text{eq}}, \quad (9)$$

where  $\varepsilon \equiv 1 - A$  is the surface emissivity. The scaling reproduces two limiting cases: (i) no atmosphere ( $\varepsilon \rightarrow 0$ ), for which  $T_{\text{surf}} = T_{\text{eq}}$ ; and (ii) a fully opaque greenhouse ( $\varepsilon \rightarrow 1$ ), for which  $T_{\text{surf}} = \sqrt{2} T_{\text{eq}}$ . For Earth-like conditions ( $\varepsilon \approx 0.78$ ), Equation 9 returns  $T_{\text{surf}} \approx 288\text{ K}$ , matching observations (Del Genio et al. 2019; McIntyre et al. 2023).

We sample a albedo interval,  $0.06 \leq A \leq 0.96$ , to capture the diversity of planetary reflectivities; note that low-albedo planets are intrinsically harder to detect because they reflect less starlight (Gaudi et al. 2020).

After drawing  $A$  and the corresponding  $\varepsilon$ , we check whether the resulting  $T_{\text{surf}}$  lies between the water freezing and boiling points at the prevailing surface pressure. The boiling curve is obtained from the Clausius–Clapeyron relation, while the freezing point is fixed at  $273.15\text{ K}$  whenever  $P_{\text{surf}} \geq P_{\text{triple}} = 611.657\text{ Pa}$ . Configurations failing this liquid-water criterion are resampled until a stable solution is found.

For every atmosphere that passes the temperature filter we assume

an isothermal vertical structure,  $T(z) = T_{\text{surf}}$ , following [Damiano & Hu \(2022\)](#), who showed that reflected-light spectra are largely insensitive to moderate vertical gradients. Pressure is divided into 60 logarithmically spaced layers over a 50-km column and declines exponentially with altitude,

$$P(z) = \exp\left(-\frac{zg_p}{R_p T_{\text{surf}}}\right) P_{\text{surf}}, \quad (10)$$

where  $g_p$  is surface gravity and  $R_p = R/M_{\text{atm}}$  is the specific gas constant, with  $R$  the universal gas constant and  $M_{\text{atm}}$  the atmospheric mean molar mass.

### 2.2.3 Cosmic Shoreline

With pressure–temperature (PT) profiles now in place, we complete the habitability filter by assessing whether an atmosphere can be retained against stellar-driven escape. An empirical boundary, the cosmic shoreline, captures this balance between incident irradiation and planetary gravity ([Zahnle 1998; Zahnle & Catling 2013, 2017](#)). In its simplest form the shoreline follows a power-law relation:

$$I_{\star} = k v_{\text{esc}}^4, \quad (11)$$

where  $I_{\star}$  is the stellar insolation defined in Equation 8,  $v_{\text{esc}} = \sqrt{2GM_p/R_p}$  is the escape velocity, and  $k = 5 \times 10^{-16} \text{ W m}^{-2} \text{ s}^4 \text{ m}^{-4}$  is an empirical constant calibrated by [McIntyre et al. \(2023\)](#). Planets that lie below the shoreline ( $I_{\star} < k v_{\text{esc}}^4$ ) are expected to retain substantial atmospheres, whereas those above it are prone to atmospheric erosion.

For each simulated planet we compute  $I_{\star}$  from its orbital distance and stellar luminosity (Equation 8) and compare the value to the threshold given by Equation 11. Roughly two-thirds ( $\approx 66\%$ ) of our configurations satisfy the retention criterion.

## 2.3 Geological epochs

The Archean atmospheric profile is based on the photochemical model from [Arney et al. \(2016\)](#). A defining feature of the Archean atmosphere is the organic haze formed via methane photolysis, which polymerizes into fractal hydrocarbon aerosols. The haze thickness is modulated by the  $\text{CH}_4/\text{CO}_2$  ratio, and [Arney et al. \(2016\)](#) investigated different ratios to simulate various haze thicknesses. Although we adopt the TP profile for  $\text{CH}_4/\text{CO}_2 = 0.21$ , we exclude explicit haze microphysics, instead allowing the mixing ratio profile to implicitly reflect haze-mediated photochemical shielding.

The Proterozoic atmospheric data were extracted from [Kawashima & Rugheimer \(2019\)](#), specifically for the post-GOE period ( $\sim 2.33$  Ga). Atmospheric oxygen levels during this epoch were approximately 0.01 present atmospheric level (PAL,  $\sim 0.2\%$  volume mixing ratio). Methane concentrations, though poorly constrained by geological records, are hypothesized to have been significantly higher than on the modern Earth.

Modern atmospheric profiles are obtained from the NASA/MERRA-2 reanalysis dataset and integrated into the Planetary Spectrum Generator (PSG) ([Gelaro et al. 2017; Villanueva et al. 2018, 2022](#)). MERRA-2 assimilates satellite and ground-station data into 72 vertical layers, with a spatial resolution of approximately 0.5 degrees. PSG refines these data to 1 km resolution using USGS-GTOPO30 topographic information and hydrostatic equilibrium assumptions. For atmospheric species not included in MERRA-2, PSG employs standard abundance profiles to fill data gaps. Further details regarding the NASA/MERRA-2 dataset can be found in [Gelaro et al. \(2017\)](#).

### 2.3.1 Mixing ratio

To capture the compositional degeneracies that often plague atmospheric retrievals, we perturb the baseline gas abundances provided by the previously described studies. For each chemical species  $i$  the perturbed mixing ratio is drawn from

$$Y_i^{\text{pert}} = Y_i^{\text{base}} \times \exp(\mathcal{U}(0, 5)), \quad (12)$$

where  $\mathcal{U}(0, 5)$  is a uniform deviate between 0 and 5. The exponent allows up to an  $e^5 \approx 150$ -fold enhancement over the baseline value, while still sampling minor depletions. After perturbation the abundances are normalized to satisfy  $\sum_i Y_i^{\text{pert}} = 1$ , thereby producing *isoabundance* profiles, vertical columns in which mixing ratios are altitude-independent. Decoupling composition from the PT structure lets any true correlations emerge organically from the data during CNN training.

The set of perturbed species varies by epoch. For the Archean template we perturb  $\text{CH}_4$ ,  $\text{H}_2\text{O}$ ,  $\text{CO}_2$ , and  $\text{N}_2$ . For the Proterozoic and Modern templates the list expands to  $\text{CO}_2$ ,  $\text{O}_2$ ,  $\text{H}_2\text{O}$ ,  $\text{O}_3$ ,  $\text{CH}_4$ , and  $\text{N}_2$ . Because we make no equilibrium-chemistry assumptions, this stochastic parameterization remains agnostic to specific reaction pathways and thus favors a fully data-driven retrieval approach.

## 2.4 Telescope properties

We generate synthetic observations for two mission concepts implemented in PSG: the 8 m coronagraphic LUVOIR-B and the 4 m starshade-assisted HabEx/SS. Both designs target a planet–star contrast of  $10^{-10}$  and we adopt the default parameters recommended in their mission reports ([The LUVOIR Team 2019; Gaudi et al. 2020](#)).

Regarding spectral coverage, LUVOIR-B observes in three bands: UV (0.20–0.515  $\mu\text{m}$ ,  $R = 7$ ), VIS (0.515–1.00  $\mu\text{m}$ ,  $R = 140$ ), and NIR (1.00–2.00  $\mu\text{m}$ ,  $R = 70$ ). HabEx/SS covers slightly shifted ranges: UV (0.20–0.45  $\mu\text{m}$ ,  $R = 7$ ), VIS (0.45–0.975  $\mu\text{m}$ ,  $R = 140$ ), and NIR (0.975–1.80  $\mu\text{m}$ ,  $R = 40$ ). PSG samples each spectrum with a boxcar kernel matched to the resolving power, and detector pixels are oversampled by a factor of ten in both spatial and spectral directions to preserve fidelity.

A key difference between the two designs lies in starlight suppression. LUVOIR-B’s internal coronagraph imposes an inner working angle of  $3.5 \lambda/D$  ([Checlair et al. 2021](#)), which corresponds to about 39 mas at 0.5  $\mu\text{m}$  and limits detection of close-in planets. HabEx/SS avoids this wavelength-dependent constraint by using an external starshade that blocks starlight at fixed angular separations (39, 58, and 104 mas in the UV, VIS, and NIR bands, respectively).

Noise modeling in PSG includes throughput losses, zodiacal light, stellar leakage, and detector noise. We assume back-illuminated CCDs with per-pixel read noise of 0  $e^-$  (UV/VIS) and 2.5  $e^-$  (NIR) for LUVOIR-B, and 0.008  $e^-$  (UV/VIS) and 0.32  $e^-$  (NIR) for HabEx/SS. Dark noise is set to  $3 \times 10^{-5} e^- \text{ s}^{-1} \text{ px}^{-1}$  (UV/VIS) and 0.002–0.005  $e^- \text{ s}^{-1} \text{ px}^{-1}$  (NIR) for LUVOIR-B and HabEx-SS, respectively ([Checlair et al. 2021](#)). Readers can find detailed equations for each noise component in [Villanueva et al. \(2022\)](#).

Instrument flags in PSG allow independent toggling of molecular, continuum, and stellar-absorption features. We enable all three for LUVOIR-B, whereas for HabEx/SS we disable stellar-absorption signatures to reflect its optically opaque starshade. Every simulation assumes a total exposure of 1000 h per planet (1000 s integrations over 3600 reads), balancing signal-to-noise ratio (SNR) against finite mission time budgets ([Checlair et al. 2021](#)). Finally, planetary geometries are randomized across 5–10 pc distances, 0–50° orbital inclinations, and orbital phases covered 0–360°.



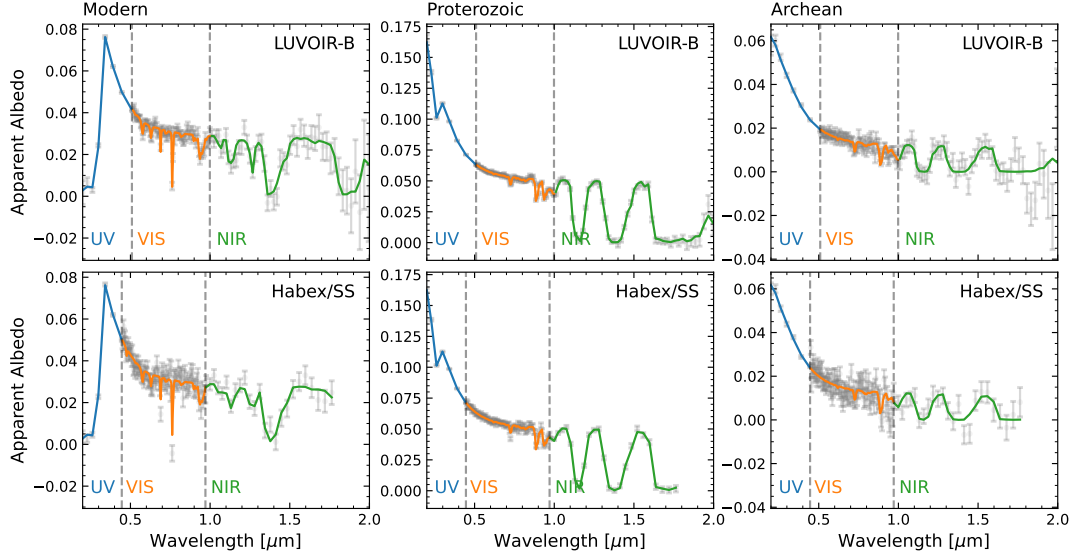


**Figure 1.** Examples of training reflection spectra for Earth-like exoplanets in the Archean (left), Proterozoic (center), and Modern (right) eras, observed with LUVIR-B (top row) and Habex/SS (bottom row). Colored lines represent the total radiance  $A(\lambda)$ , while points with error bars correspond to  $A_{\text{noisy}}(\lambda)$  as defined by Equation 13.

## 2.5 Sample selection

The physical and observational filters described above greatly restrict the available parameter space. Although a majority of planets below the cosmic shoreline can in principle retain an atmosphere, we find that only about 15% also satisfy the simultaneous PT requirements for surface liquid water. Given this low occurrence rate, we adopted a recursive sampling method: up to 200 iterations are performed per target, each drawing a fresh combination of stellar, orbital, planetary, atmospheric, and instrument parameters. For every draw a configuration file is generated, all PSG modules are executed, and the resulting total-radiance spectrum is returned. The first column of each output file lists wavelength in  $\mu\text{m}$ , followed by the apparent-albedo spectrum  $A(\lambda)$ , the noise array  $\sigma(\lambda)$ , and the individual radiative sub-components.

Before retaining a spectrum, we impose one last cut. Because the noise is modeled as Gaussian, the probability that a genuine signal deviates from its noiseless value by more than three standard deviations is only 0.3%. We therefore reject any spectrum for which the noise at any wavelength exceeds the  $3\sigma$  threshold. For every sample that passes this cut, the noisy spectrum used for training,  $A_{\text{noisy}}(\lambda)$ , is produced by drawing from a normal distribution centered on the noiseless radiance with the standard deviation at that wavelength,

$$A_{\text{noisy}}(\lambda) \sim \mathcal{N}(A(\lambda), \sigma(\lambda)). \quad (13)$$

Out of more than 3.7 million computed samples, only 1,086,914 exoplanets met all the requirements, forming the final dataset used in this work. This sample is evenly divided among the three geological eras, so that roughly one-third of the spectra represents each epoch. Examples of these synthetic spectra are shown in Fig. 1.

The planetary parameters (radius, gravity, surface temperature, and surface pressure) are sampled uniformly within the ranges listed in Table 1, irrespective of geological epoch. Atmospheric compositions, on the other hand, follow the log-uniform perturbation scheme of Equation 12 and are constrained to the order of magnitude bounds given in Table 2. For epochs in which certain species are geologically implausible ( $\text{O}_2$ , and  $\text{O}_3$  in the Archean), fixed zero abundances are assigned, explicitly indicating their absence.

**Table 1.** Planetary parameter space adopted for uniform sampling.

| Parameter                         | Min | Max  |
|-----------------------------------|-----|------|
| Planetary radius ( $R_{\oplus}$ ) | 0.6 | 1.2  |
| Planet gravity ( $\text{m/s}^2$ ) | 4.2 | 13.9 |
| Atmosphere temperature (K)        | 273 | 383  |
| Atmosphere pressure (mbar)        | 172 | 2047 |

**Table 2.** Order of magnitude bounds for gas mixing ratios in each geological epoch.

| Parameter            | Archean   |           | Proterozoic |           | Modern    |           |
|----------------------|-----------|-----------|-------------|-----------|-----------|-----------|
|                      | Min       | Max       | Min         | Max       | Min       | Max       |
| $\text{CH}_4$        | $10^{-5}$ | $10^{-1}$ | $10^{-5}$   | $10^{-1}$ | $10^{-8}$ | $10^{-4}$ |
| $\text{CO}$          | $10^{-5}$ | $10^{-1}$ | $10^{-7}$   | $10^{-3}$ | $10^{-8}$ | $10^{-4}$ |
| $\text{H}_2\text{O}$ | $10^{-6}$ | $10^{-2}$ | $10^{-5}$   | $10^{-1}$ | $10^{-6}$ | $10^{-2}$ |
| $\text{N}_2$         | $10^{-1}$ | $10^0$    | $10^{-1}$   | $10^0$    | $10^{-2}$ | $10^0$    |
| $\text{O}_2$         | Fixed (0) |           | $10^{-5}$   | $10^{-1}$ | $10^{-3}$ | $10^0$    |
| $\text{O}_3$         | Fixed (0) |           | $10^{-10}$  | $10^{-6}$ | $10^{-8}$ | $10^{-4}$ |

## 3 NEURAL NETWORK TRAINING

Our models were trained and tested using the TensorFlow interface (Abadi et al. 2015). In this section, we briefly introduce the general concept of 1D CNNs, describe how our dataset is organized to maximize training efficiency, and present the proposed network architecture in detail.

### 3.1 1D CNN concept

The data generation discussed in the previous section feeds into an ML model. Broadly, ML is the systematic effort to build algorithms that transform inputs (features) into useful outputs, and in supervised tasks this transformation is learned from labeled data rather than hand-crafted rules.

DL implements this idea through many stacked, trainable layers that progressively extract higher-level representations of the input. Within the DL family, fully connected (dense) networks constitute one canonical architecture: each layer first applies an affine transformation and then passes the result through a non-linear activation (Bishop 2006). Formally, if  $\mathbf{A}^{(\ell-1)}$  denotes the input to layer  $\ell$ , the output becomes

$$\mathbf{A}^{(\ell)} = \phi \left( \mathbf{W}^{(\ell)} \mathbf{A}^{(\ell-1)} + \mathbf{b}^{(\ell)} \right), \quad (14)$$

where  $\mathbf{W}^{(\ell)}$  and  $\mathbf{b}^{(\ell)}$  are the trainable weights and biases, respectively, and  $\phi$  is an element-wise activation function. During training, these parameters are iteratively updated so as to minimize a cost function. In this work we adopt the mean absolute error (MAE) as the cost function,

$$\text{MAE} = \frac{1}{ND} \sum_{n=1}^N \sum_{d=1}^D |y_{n,d} - \hat{y}_{n,d}|, \quad (15)$$

with  $N$  the number of samples,  $D$  the dimensionality of the target vector,  $y_{n,d}$  the ground-truth value and  $\hat{y}_{n,d}$  the model prediction.

Although dense layers can model arbitrary interactions, they do not encode the fact that neighboring wavelengths tend to be correlated, because every weight is learned without regard to positional proximity. To inject this inductive bias we turn to 1D CNNs (LeCun et al. 1989; Rumelhart et al. 1985). In a 1D CNN each convolutional kernel  $k$  (or filter) consists of multiple vectors  $\mathbf{w}_{k,c} = \{w_{k,0}, \dots, w_{k,h-1}\}$  (one per input channel  $c$ ) of length  $h$  that slides along the spectrum and acts as a learnable window over adjacent wavelength bins. Applying these kernels to the activations of the previous layer produces a set of *feature maps*. Formally, the feature map of output channel  $k$  at layer  $\ell$  is given by

$$\mathbf{A}_k^{(\ell)} = \phi \left( \sum_c \mathbf{w}_{k,c}^{(\ell)} * \mathbf{A}_c^{(\ell-1)} + b_k^{(\ell)} \right), \quad (16)$$

where the symbol  $*$  denotes cross-correlation (not a mathematical convolution) and the sum runs over all input channels  $c$ . Because the same kernel coefficients are reused at every position, this weight sharing both reduces the number of parameters and makes the network translation-equivariant along the wavelength axis, i.e., sensitive to local motifs but agnostic to their absolute location.

Finally, pooling layers down-sample these feature maps by taking local statistics, typically a maximum or an average, thereby promoting invariance to small shifts while enabling deeper layers to integrate information over progressively broader spectral regions.

### 3.2 Dataset structure

The generated final sample was first stored as column-oriented parquet files containing the complete PSG configuration for each planet. For neural-network training we retained only the wavelength-dependent apparent albedo, the corresponding noise array, the noisy albedo (Equation 13) for both LUVOR-B and HabEx-SS simulations and desired targets. These reduced tables were converted to TensorFlow's TFRecord format, which serializes each example as a Protocol-Buffers message and enables efficient streaming, shuffling, and prefetching in input pipelines.

Within every TFRecord example the input tensor is organised as three one-dimensional arrays (UV, VIS, and NIR) matching the spectral bands defined in Section 2.4. The target vector is partitioned into *Physical Features* (PF), *Main Chemical Features* (MCF), and *Other Chemical Features* (OCF). PF comprises planetary radius, surface

gravity, surface temperature, and surface pressure. MCF contains only  $\text{O}_2$  and  $\text{O}_3$ , molecules singled out both for their diagnostic spectral signatures in the UV/VIS and for their relevance as primary biosignatures in modern Earth-like atmospheres. OCF includes all remaining gases listed in Table 2. This hierarchical target structure is identical for the LUVOR-B and HabEx-SS datasets.

To prevent data leakage and maintain data balance, the dataset is split by epoch into training (80%), validation (10%), and test (10%). Because each epoch contributes the same fractional split, the final three files preserve the original ratio and ensure that no spectrum from a given planet appears in more than one subset.

### 3.3 Normalization I/O

Neural-network training is greatly facilitated when each input channel and target variable occupies a similar numerical range. Without such normalization, features with large dynamical ranges can dominate the gradient updates and hinder convergence, while highly skewed target distributions may bias the loss landscape. We therefore apply three complementary scaling strategies tailored to the statistical properties of (i) spectra, (ii) PF targets, and (iii) MCF and OCF targets. In every case the required statistics are computed *only* on the training set and then reused, without modification, for the validation and test splits.

For every spectrum the noisy apparent albedo  $A_{\text{noisy}}(\lambda_j)$  is standard scaler normalized,

$$\bar{A}_{\text{noisy}}(\lambda_j) = \frac{A_{\text{noisy}}(\lambda_j) - \langle A_{\text{noisy}}(\lambda_j) \rangle}{\sigma_i}, \quad (17)$$

where the brackets denote the sample mean across the training set and  $\sigma_j$  is the corresponding standard deviation at wavelength bin  $\lambda_j$ .

The PF targets are each rescaled by a min–max transformation,

$$\bar{y}_{ij} = \frac{y_{ij} - \min(y_{ij})}{\max(y_{ij}) - \min(x_{ij})}, \quad (18)$$

where  $y_{ij}$  is the raw value of variable  $i$  for sample  $j$  and the extrema are computed over the entire training set (ranges given in Table 1).

The MCF and OCF targets span up to eight orders of magnitude (Table 2) and include true zeros for species in the Archean era. Direct logarithms are therefore unusable:  $\log 0$  is undefined, and very large abundances would collapse toward  $\log 1 = 0$ . To mitigate this double-zero problem, we adopt a power-law mapping inspired by the *Hellinger transform* (Legendre & Gallagher 2001; Conde & Domínguez 2018),

$$\bar{H}_{ij} = (p_{ij})^{1/n_i} \quad \text{where} \quad p_{ij} = \frac{y_{ij}}{\sum_i y_{ij}}, \quad (19)$$

where  $y_{ij}$  is the raw count of species  $i$  in sample  $j$ , and  $n_i > 0$  is a species-specific exponent. Increasing  $n_i$  stretches the low-abundance tail, whereas decreasing it compresses high values; choosing  $n_i = 1$  leaves the distribution unchanged. For each chemical species we scanned  $n_i \in [0.05, 50]$  and selected the exponent that maximized the spread of the transformed histogram ( $\theta_1$ ) while, in the event of degeneracy, also maximizing its total area ( $\theta_2$ ). The same procedure was applied to surface temperature, whose distribution remained skewed even after min–max scaling. Best values of  $n_i$  are listed in Table 3 and the selection process is illustrated in Fig. A1 of the appendix.

### 3.4 Network architecture

Fig. 2 shows our best CNN's architecture adopted in this work. The same layout is used for both telescope; the only difference is the

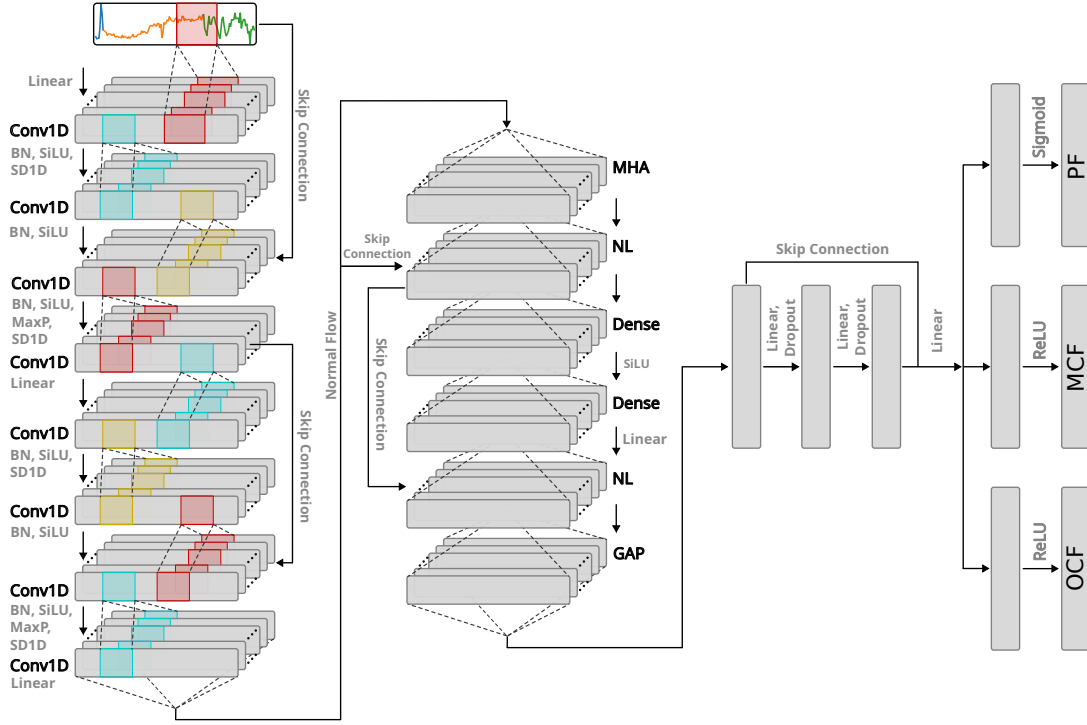


**Figure 2.** General concept of the best CNN’s architecture. The data flow starts in the top left part of the scheme, with a convolution over the spectrum. The flow goes down through the 1D convolutional layers until reach the Conv1D layer in the bottom left part, passing through Batch Normalization (BN), SiLU activation functions, SpatialDropout1D (SD1D) and MaxPooling (MaxP) as indicated. We added skip connections as indicated so that the data flow in both forward and back propagation is enhanced. After the last Conv1D layer, the we added a Multi-Head Attention (MHA) layer, followed by a Normalization Layers (NL), dense layers and a Global Average Pooling (GAP) as indicated. A set of dense layers follows, until the network forks its outputs into dense layers branches for the *Physical Features* (PF), *Main Chemical Features* (MCF) and *Other Chemical Features* (OCF). The same network architecture was used for both LUV0IR-B and HabEx/SS data cases, with different numerical specifications for layers, sizes and so on, so we omitted all of these informations.

**Table 3.** Best  $n$  values for each parameter considered.

| Best $n$  | CH <sub>4</sub> | CO <sub>2</sub> | H <sub>2</sub> O | N <sub>2</sub> | O <sub>2</sub> | O <sub>3</sub> | $T_{\text{atm}}$ |
|-----------|-----------------|-----------------|------------------|----------------|----------------|----------------|------------------|
| Parameter | 6.65            | 3.65            | 4.80             | 0.35           | 2.35           | 13.80          | 2.52             |

dimensionality of the input spectral vector. HabEx/SS spectra yield a concatenated sequence of  $L_H = 141$  points (7 UV, 109 VIS, 25 NIR), whereas LUV0IR-B spectra give  $L_L = 151$  points (8 UV, 94 VIS, 49 NIR).

The spectral sequence first passes through two residual convolutional blocks. In each block the input is convolved twice with 1-D filters, each convolution followed by batch normalization (BN), the SiLU activation

$$\phi_{\text{SiLU}}(x) = \frac{x}{1 + e^{-x}}, \quad (20)$$

and a spatial dropout (SD1D) mask that randomly zeroes entire feature channels with probability  $p_D$  during training. Spatial dropout preserves temporal coherence while acting as strong regularizer. The double-convolved tensor is added to the block input to form the skip connection, then a final strided convolution halves the sequence length. Kernel sizes are drawn from  $h_1 \in \{L/4, L/3\}$  for the first block and  $h_2 \in \{L/2, 3L/4, L\}$  for the second, let the network detect both local and near-global spectral features.

Convolutions capture short-range correlations but can miss broader dependencies. To address this, the network is followed by a multi-head self-attention (MHA) layer (for further details, see Géron (2022)). In self-attention the same spectral sequence is lin-

early projected three times to form *queries*, *keys*, and *values*. Each query represents a wavelength bin that is “asking” how strongly it should attend to every other bin; the corresponding keys provide the information needed to answer that question, while the values carry the spectral content that will ultimately be combined. The inner product between a query and the keys, scaled by the key dimension  $d_{\text{keys}}$ , yields the attention weights, a probability distribution that tells the network where to look across the entire spectrum. Running this operation in parallel over  $q$  distinct query–key–value sets lets the model track several wavelength–interaction patterns at once; the pair  $(q, d_{\text{keys}})$  therefore defines the “transformer capacity” tuned during hyperparameter optimization. The attention output is added back to its input via a residual link and then normalized (NL), ensuring stable gradients before the data flow continues to the dense layers.

A global average pooling (GAP) layer compresses the attended sequence to a latent vector. Three fully connected layers of  $u$  units each further transform this representation; after every affine transform a standard dropout mask with rate  $p_D$  is applied, and the shortcut from the first dense layer is added back to form an additional residual path.

The network then splits into three heads. The PF head predicts the four bulk quantities and uses the sigmoid function,

$$\phi_{\text{Sigmoid}}(x) = \frac{1}{1 + e^{-x}}, \quad (21)$$

to keep each value in  $[0, 1]$  before inverse scaling. The MCF and OCF heads use a clipped ReLU,

$$\phi_{\text{ReLU}}(x) = \max(0, x), \quad (22)$$

capped at unity, which guarantees non-negative mixing ratios. MAE

**Table 4.** Best hyperparameters and training outcomes for HabEx/SS and LUVOIR-B after Bayesian optimization.

| Parameter                                   | HabEx/SS | LUVOIR-B |
|---|----------|----------|
| Filters                                     | 56       | 56       |
| Kernel length $h_1$                         | 35       | 50       |
| Kernel length $h_2$                         | 141      | 151      |
| Key dimension $d_{\text{keys}}$             | 16       | 16       |
| Transformer capacity $(q, d_{\text{keys}})$ | 4        | 2        |
| Dense units $u$ (first dense) <sup>5</sup>  | 16       | 32       |
| Dropout $p_D$                               | 0.35     | 0.25     |
| Learning rate                               | 0.001    | 0.001    |
| Training time (min)                         | 41       | 39       |
| Validation loss MAE <sub>total</sub>        | 0.2568   | 0.2392   |
| Validation loss MAE <sub>PF</sub>           | 0.0995   | 0.0893   |
| Validation loss MAE <sub>MCF</sub>          | 0.0337   | 0.0315   |
| Validation loss MAE <sub>OCF</sub>          | 0.0599   | 0.0580   |

losses from the three heads are combined with weights of 1:2:1.5, emphasizing O<sub>2</sub> and O<sub>3</sub> retrievals.

All remaining hyper-parameters, such as filter count, kernel lengths ( $h_1$ ,  $h_2$ ), key dimension ( $d_{\text{keys}}$ ), transformer capacity ( $q$ ,  $d_{\text{keys}}$ ), dense units  $u$ , dropout  $p_D$ , and Adam learning rate, were tuned separately for each telescope with Bayesian optimization (O’Malley et al. 2019). Thirty trials were run, and each trial was trained for three epochs to obtain a reliable validation loss estimate without excessive cost. After ranking the trials, the best configuration was re-initialized and trained from scratch for 50 epochs. Three callbacks were used during this final training: TensorBoard, to enable real-time diagnostics; ReduceLROnPlateau, which reduced the learning rate by a factor of 0.6 whenever the validation loss stagnated for five epochs; and EarlyStopping, configured to halt training if no improvement occurred in ten consecutive epochs, though this condition was never met, as all runs completed the full 50 epochs.

The complete set of best hyper-parameters, together with run-time and validation performance, are listed in Table 4. The final LUVOIR-B model contains 5.28 million parameters in total, while the HabEx/SS model contains 4.72 million parameters. Both networks were trained with a mini-batch size of 1024 on an NVIDIA A100 GPU hosted on Google Colaboratory. Our full implementation is openly available on GitHub<sup>4</sup>.

## 4 RESULTS AND DISCUSSION

The analysis below examines how well the trained networks perform on the test set, spectra they never “saw” during optimization. The numbers that follow therefore probe the model’s true ability to generalize.

### 4.1 Predicted versus true values

For every planetary feature we compare the predicted values,  $\hat{y}_i$ , with the true ones,  $y_i$ , in the one-to-one scatter plots for chemical abundances (Fig. 3) and for physical parameters (Fig. 4). The test set was first stratified by geological era so we could see how the model responds to different abundance scales. Because the mixing ratios span

up to 11 orders of magnitude (see Table 2), we analyze the abundances in log space after de-normalizing (i.e., inverting transforms (18) and (19)); rows whose true value is exactly zero are discarded before taking the logarithm.

One way to quantify the agreement between predicted and true values is to use the coefficient of determination (Pedregosa et al. 2011),

$$R^2 = 1 - \frac{\sum_i (y_i - \hat{y}_i)^2}{\sum_i (y_i - \bar{y})^2}, \quad (23)$$

where  $\bar{y}$  is the mean of the true values. This metric can be read as the ratio between the model’s prediction residuals and the total sum of squares; values near 1 are ideal because they track the correlation between predicted and true parameters. This information is also shown in each panel of the figures mentioned above, where we adopted  $R_L^2$  for LUVOIR-B and  $R_H^2$  for HabEx/SS. Although both have different values, the trend behavior is similar.

The network performs best on spectroscopically “bright” species. Performance, as expected, depends on era: CH<sub>4</sub>, for example, is recovered very accurately in Archean atmospheres but much worse in modern compositions. The modern subset covers a narrow dynamic range dominated by low CH<sub>4</sub>; the network, trained on a balanced mix, tends to overestimate those small values, yielding an apparently negative score. A similar, though milder, trend appears for CO<sub>2</sub>.

Nitrogen is spectrally dull in the VIS/near-IR and is therefore intrinsically harder. The network only reproduces its logarithmic abundance in a statistical sense; individual predictions scatter symmetrically around the 1:1 line with a dispersion of  $\approx 0.2$ .

O<sub>2</sub> is retrieved with good accuracy when all samples are considered together, though performance varies by era. As expected from its greater present-day abundance, O<sub>3</sub> is predicted well in modern atmospheres by both instruments. However, the models perform poorly for the Proterozoic era, yielding negative  $R^2$  scores. Furthermore, the O<sub>2</sub> and O<sub>3</sub> results show a long tail of extreme outliers. In cases where the model attempts to infer a complete absence of these gases (such as in the Archean), it generates very low log-values, close to  $-40$ .

For these truly zero-abundance cases we computed summary statistics of the predictions. The median confirms that zero is the modal outcome, as expected given the presence of ReLU on the OCF and MCF head. O<sub>3</sub> is essentially zeroed out: the mean ( $\mu_L \approx 10^{-9}$  and  $\mu_H \approx 10^{-10}$ ) and dispersion ( $\sigma_H = \sigma_L \approx 10^{-8}$ ) sit eight orders of magnitude below the non-zero values used during training. O<sub>2</sub> shows a slightly larger spread ( $\mu_L = \mu_H \approx 10^{-4}$ ,  $\sigma_H = \sigma_L \approx 10^{-3}$ ), yet even that lies two orders of magnitude below the modern Earth level (0.21). In other words, when the spectrum carries no information about a molecule, the network consistently outputs a numerically negligible value without any *ad-hoc* detection threshold. The CNN therefore behaves as a conservative estimator: when the spectral fingerprint is silent, so is its prediction.

Turning to the planetary parameters (we omit the era-by-era plots because they have the same tendency), radius, gravity, and pressure are recovered with high accuracy and negligible bias. Their diagonal stripes are nearly dispersion-limited, confirming that continuum level and spectral amplitude carry ample information on scale height. By contrast, atmospheric temperature shows a nearly tight scatter plot yet attains only low score. The apparent paradox arises because the dynamic range is small (see Table 1): even a  $1\sigma \approx 20$  K error looks small on the density plot but dominates the variance term in the  $R^2$  denominator. Residuals are almost homoscedastic, suggesting that temperature errors do not strongly propagate into the other retrieved quantities.

Although we do not present the results here, we did attempt to

<sup>4</sup> <https://github.com/SarahBarbosa/geexhp>



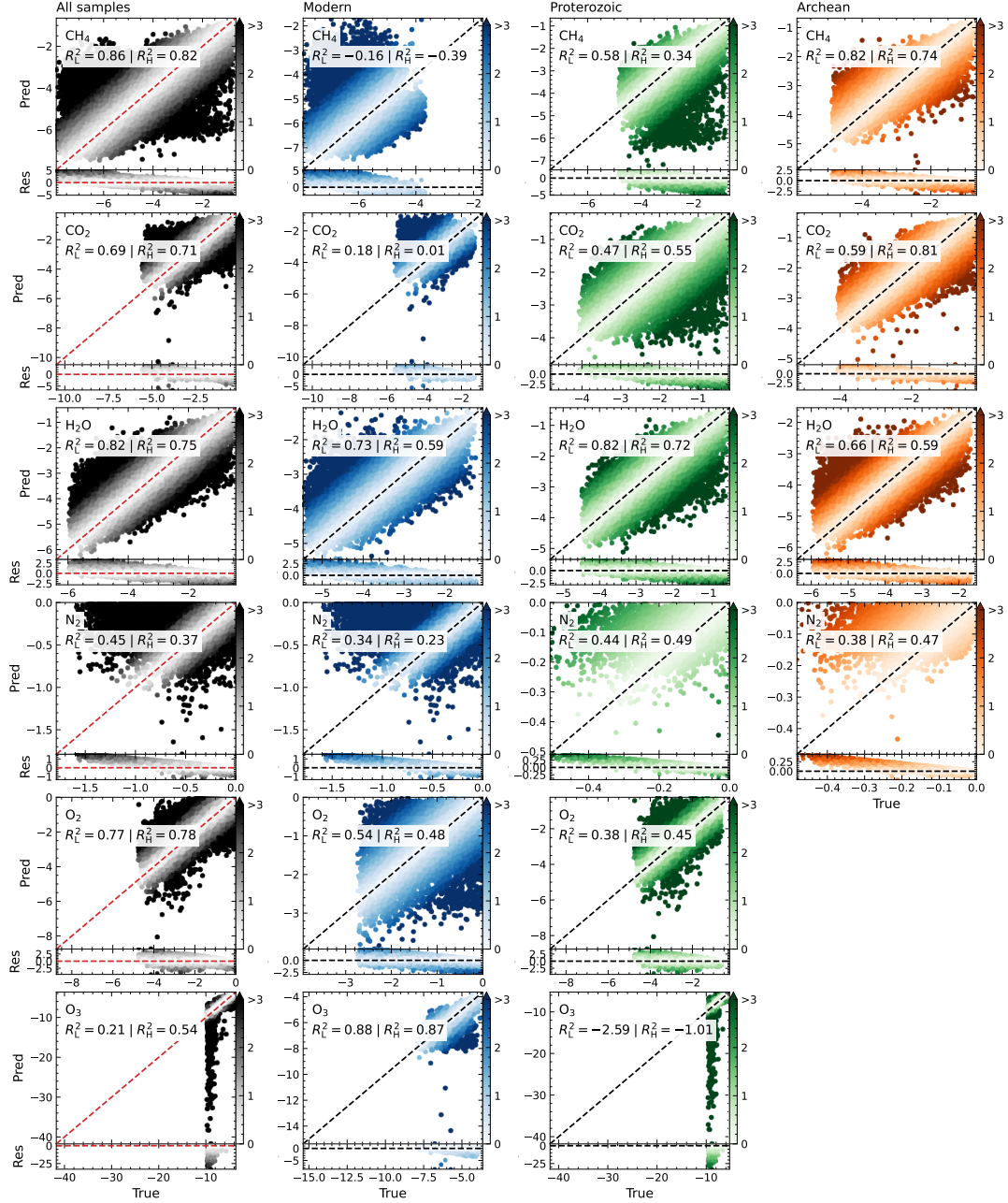


**Figure 3.** Predicted versus true  $\log_{10}$  abundances for the test set. Panels are organized by geological era (columns) and molecule (rows). Marker color shows the sigma-away metric clipped at 3 after excluding  $y_i = 0$ . The dashed line marks the ideal case  $y_i = \hat{y}_i$ , and the lower inset of each panel displays the residuals. In-panel labels report  $R_L^2$  for LUVOIR-B and  $R_H^2$  for HabEx/SS; although these  $R^2$  values are different, the overall pattern of dispersion and residual structure are similar between the two instruments.

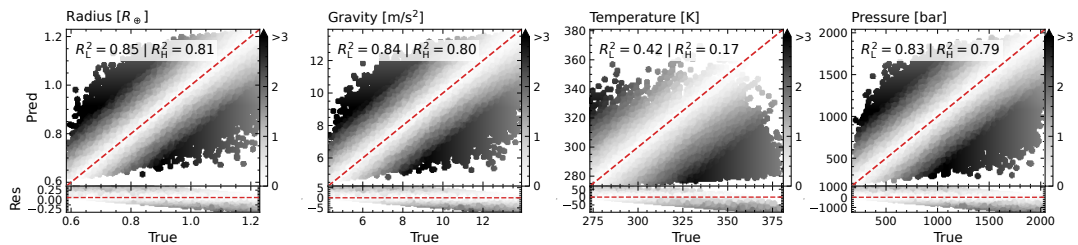


**Figure 4.** Same layout as Fig. 3, now for planetary radius, surface gravity, atmosphere temperature, and atmosphere pressure for all test set.

retrieve CO and N<sub>2</sub>O. The CNN failed. Our perturbation (Equation 12) scales the mixing ratios randomly by up to a factor of 150. This spread is sufficient for molecules whose strong bands imprint clear morphological changes on the reflection spectra, because it supplies the network with genuinely diverse inputs. CO and N<sub>2</sub>O, however, exhibit intrinsically weak absorption within the wavelength range considered. Even a two-order-of-magnitude increase scarcely alters the synthetic spectra, leaving the inputs nearly degenerate and driving the network toward misleading mappings; the resulting coefficients of determination fall below zero. To prevent this degeneracy from polluting the overall performance metrics, we omit these two species.

#### 4.2 Uncertainty estimation via Monte Carlo Dropout

To estimate parameter uncertainties, we employed the Monte Carlo Dropout method (Gal & Ghahramani 2015). This technique transforms our deterministic model into a stochastic ensemble by keeping dropout layers active during inference. For each input spectrum, we perform  $T$  stochastic forward passes, generating a distribution of predictions. From this distribution, we calculate the predictive mean (our final parameter estimate) and the predictive variance (which quantifies the model’s uncertainty). Given our CNN architecture, we specifically used SpatialDropout1D after the convolutional layers, as standard dropout is ineffective on correlated feature maps (Tompson et al. 2014), and applied conventional dropout only after the dense layers.

Once the predictive distributions are obtained, we must assess model performance across the full test set, which contains 87,419 spectra. Generating corner plots for all of them is computationally infeasible and analytically uninformative. To overcome this, we compute the Euclidean distance ( $D$ ) between the true parameter vector  $y$  and the predictive mean from each telescope model. Since the parameters were already standardized, this metric reflects relative deviations fairly across dimensions.

By ranking the distances, we identify the spectra for which each model performs best (smallest  $D$ ) and worst (largest  $D$ ). We then select the example whose true value lies closest to the predictive means of both telescope models, representing a case where both models independently approximate the ground truth with high accuracy. Fig. 5 displays the resulting posterior distribution for this optimal case in the Modern era (after  $T = 5000$ ). The corresponding best cases for the Proterozoic and Archean scenarios, as well as the worst-performing prediction across the dataset, are presented in the appendix (Figures A2, A3, and A4, respectively).

As we can see, in the best Modern Earth case, LUVOIR-B and HabEx/SS models managed to predict within  $1\sigma$  of the ground truth values (as indicated by the dashed blue line for LUVOIR-B and dashed black line for HabEx/SS). Moreover, they successfully captured some expected correlations, such as  $R$  versus  $P$  and  $g$  versus  $P$ .

Interestingly, a distinctive feature emerges in the Modern Earth sample that is absent from the other geological eras: a clear negative correlation between N<sub>2</sub> and O<sub>2</sub>. This degeneracy arises from the fact that N<sub>2</sub> lacks strong spectral features, making it difficult to detect directly. Yet both N<sub>2</sub> and O<sub>2</sub> are highly abundant in the modern atmosphere. Thus, when balancing the total atmospheric composition, the model must account for the simultaneous presence of both gases. The negative correlation indicates that as the model sees an increase in the abundance of N<sub>2</sub>, it necessarily decreases O<sub>2</sub> to maintain the overall compositional equilibrium enforced by the simulation.

To assess performance on the full test set, we computed, for every spectrum, the absolute deviation between the posterior mean and the

true value of each retrieved quantity and then recorded the proportions of samples contained within  $\pm 1\sigma$ ,  $\pm 2\sigma$  and  $\pm 3\sigma$ . Fig. 6 shows that coverage increases monotonically with interval width across all eras and for both telescopes, confirming that the predicted posteriors are informative. Even so, every curve lies below the Gaussian expectations of 68.3 %, 95.4 % and 99.7 %, implying that the uncertainty estimates are systematically too narrow. As noted earlier, the network struggles most with temperature; its coverage never exceeds 20 % for any era or instrument. The near-unit coverages of O<sub>2</sub> and O<sub>3</sub> in the Archean subset are artifacts of both abundances being intrinsically zero, which truncates the posteriors at the physical lower bound rather than reflecting genuine spectral constraints. Overall, more than half the test spectra fall within  $\pm 2\sigma$  for every other retrieved quantity (radius, gravity, surface pressure, and all molecular abundances), while temperature remains below this threshold.

#### 4.3 Feature importance via Integrated Gradients

To understand which spectral features our model uses for its predictions, we employed the Integrated Gradients (IG) technique, an explainable AI (XAI) method proposed by Sundararajan et al. (2017). This method attributes the prediction for each gas to individual input features (i.e., wavelengths) by calculating the model’s gradients along a linear path from a baseline to the input spectrum. For our analysis, we defined the baseline as a null albedo spectrum, representing the absence of planetary reflection. The final output is an importance curve,  $IG_g(\lambda)$ , for each gas, which maps the relevance of each point in the spectrum for that gas’s prediction.

To illustrate this, we select one random test spectrum from each geological era and run the IG analysis with LUVOIR-B and HabEx/SS. Figure 7 compares the two instruments across three wavelength bands that track Earth’s atmospheric evolution. In the modern Earth case, the network assigns greater importance to the Fraunhofer A band at  $0.76\ \mu\text{m}$  and a part of the UV, corresponding to the expected O<sub>2</sub> absorption. This feature is sharper in LUVOIR-B than in HabEx/SS because LUVOIR’s VIS channel has lower photometric noise, as seen in the scatter of open circles. The response for O<sub>3</sub> appears almost exclusively in the UV, in line with the Hartley–Huggins band. LUVOIR-B also assigns a negative contribution to N<sub>2</sub> near  $0.76\ \mu\text{m}$ , implying that this gas partly offsets the positive O<sub>2</sub> signal.

The Proterozoic example pushes the model toward its detection threshold. LUVOIR-B drives the corresponding IG curves almost to zero, effectively declaring the gases absent. HabEx/SS, however, gives non-trivial weight to O<sub>2</sub> in UV band. In LUVOIR-B the weak O<sub>2</sub> signal leaves room for a misleading positive attribution to CO<sub>2</sub> ( $IG \approx 0.15$ ) and once again a negative dip in N<sub>2</sub> at  $0.76\ \mu\text{m}$ . These cross-gas effects indicate that when biosignature bands carry little information the model shifts relevance to correlated absorbers, which can produce false positives.

The Archean scenario, conversely, displays the opposite trend: Rayleigh scattering enhances the UV continuum, causing reflectance to drop steeply beyond  $0.35\ \mu\text{m}$ . Consequently, both telescopes assign most of their IG to this UV region. LUVOIR-B directs this importance specially to N<sub>2</sub> absorption, but HabEx/SS misattributes significant relevance to O<sub>2</sub> and O<sub>3</sub>, despite their complete absence in Archean atmospheres. This erroneous attribution arises from the zero-baseline IG method: when a bright feature is present in the input, saturation effects in the gradients can spread to nearby wavelengths, artificially inflating importance scores in spectral regions devoid of actual molecular features.

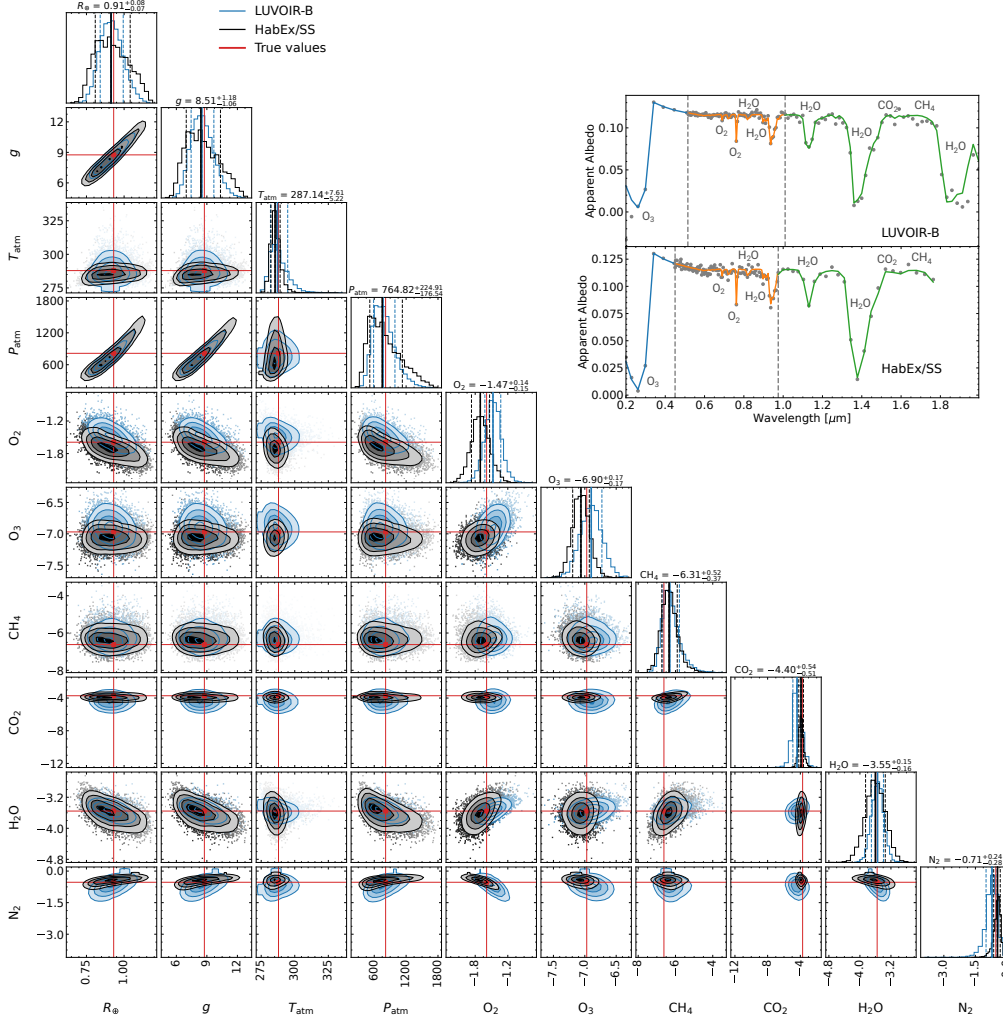


**Figure 5.** Posterior distribution for a Modern Earth sample from the test set, obtained after  $T = 5000$  Monte Carlo draws. This corresponds to the spectrum whose true parameter vector lies closest, in Euclidean distance, to the predictive means of both the LUVOIR-B and HabEx/SS trained models. Blue contours and histograms denote the LUVOIR posterior, black represents the HabEx posterior, and red lines mark the true parameter values (with the dotted lines indicating the  $\pm 1\sigma$  intervals). Molecular abundances are shown in logarithmic scale. The inset shows the observed spectrum for this sample.

#### 4.4 Credibility horizons for $O_2$ and $O_3$

To assess how much trust an observer can place in a single CNN prediction, we follow the credibility limit described by Yip et al. (2021). For a molecule with true log-abundance  $Y$  and network estimate  $\hat{Y}$ , they define the *credibility probability* as,

$$\mathcal{P}_\varepsilon(\hat{Y}) = \Pr\left(|Y - \hat{Y}| \leq \varepsilon \mid \hat{Y} = \hat{y}\right), \quad (24)$$

that is, the fraction of test spectra for which the absolute error does not exceed a tolerance  $\varepsilon$  when the network predicts a value within a narrow bin centered at  $\hat{y}$ . A prediction level is deemed credible if  $\mathcal{P}_\varepsilon > 1 - \delta$ ; by scanning from high to low predicted abundances, the lowest  $\hat{y}$  that satisfies this condition defines the credibility limit  $L_{\delta, \varepsilon}$  (for further details, see Yip et al. (2021)).

Here, we adopt the same parameters used by the authors:  $\varepsilon = 0.5$ ,  $\delta = 0.3$ , fixed-width bins of 0.5, and a minimum of 20 spectra per bin. We then compute  $\mathcal{P}_\varepsilon$  for every  $O_2$  and  $O_3$  prediction produced by our networks in a sample from the test set, after removing any spectrum whose true or predicted mixing ratio was exactly zero (Figures 8 and 9).

For  $O_2$  (left column of Fig. 8), the credibility curves increase

steadily with abundance. Around all spectral type stars, both conceptual telescopes cross the 0.7 threshold as soon as the network predicts a mixing ratio of  $\geq -2$ . The distance-based slices tell a similar story (left column of Fig. 9). Up to about 8–10 pc, both instruments retain credibility down to mixing ratio of  $-2$ , but as the planet–telescope separation stretches to 18–20 pc, the limit brightens toward  $-1$ , a direct indication that photometric noise, rather than model bias, defines the horizon. Yip et al. (2021) warned that sparsely populated bins can feign high probabilities; our  $\geq 20$ -spectra/bin requirement mitigates this issue, and the smoothness of the gray (LUVOIR-B) and black (HabEx/SS) curves confirms that the trend is not a small-sample artifact.

In stark contrast,  $O_3$  (right columns of Figures 8 and 9) proves almost indifferent to stellar type or distance. Every slice maintains  $\Pr(|\text{error}| \leq 0.5) \gtrsim 0.85$  across the full explored range of log-abundances. Minor fluctuations, such as in the 16–18 km slice where HabEx/SS briefly dips below LUVOIR-B, remain well above the 0.7 line and fall within the 5% statistical scatter already reported by Yip et al. (2021) for this probability regime.

Taken together, these curves delineate two distinct retrievability

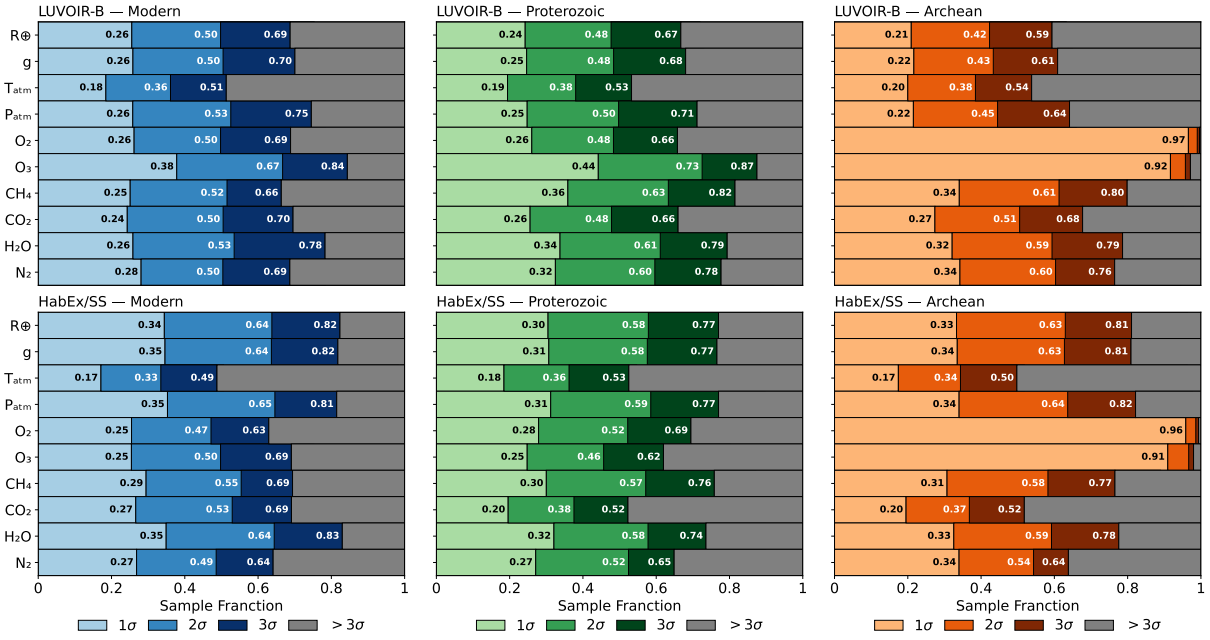


**Figure 6.** Comparison of parameters retrievals for LUVOR-B and HabEx/SS for different  $\pm\sigma$  ranges extracted from an analysis like in Fig. 5 of the whole test set.

horizons. First,  $O_2$  is reliably retrievable down to a 1.5% mixing ratio for FG stars within 10–12 pc, and to 2% at 8–10 pc for K hosts; below those levels, both networks regress toward a noise-driven prior. Second, ozone exhibits a much deeper horizon: neither the host spectrum nor the photon budget compromises its credibility within the simulated bounds, setting our practical floor at  $-9$  threshold imposed by the dataset, not by instrumental sensitivity.

## 5 CONCLUSIONS

This work presents a novel application of a one-dimensional CNN for the simultaneous retrieval of six molecular mixing ratios ( $CH_4$ ,  $CO_2$ ,  $H_2O$ ,  $N_2$ ,  $O_2$ ,  $O_3$ ) and four planetary parameters (radius, gravity, surface pressure, and surface temperature). The model was applied to reflection spectra of Earth-like exoplanets generated for the Archean, Proterozoic, and Modern eras. Trained on over one million noise-injected synthetic spectra from the Planetary Spectrum Generator for LUVOR-B and HabEx/SS, our model achieves inference in mere seconds for 5,000 Monte Carlo Dropout samples on a single RTX 2060 GPU. These results establish the architecture as a viable and practical alternative to traditional Bayesian methods, which often require runtimes of hours to days.

The model’s performance is strongest where spectral signatures are prominent, such as for  $CH_4$  and  $CO_2$  in the Archean era, and for  $O_2$  and  $O_3$  in the Modern era. As expected, performance degrades as spectral lines weaken.  $N_2$  remains challenging to retrieve due to its intrinsically faint features in the VIS/NIR range, while  $O_2$  and  $O_3$  in the Proterozoic era yield negative  $R^2$  scores. Critically, in cases of true zero-abundance (e.g., Archean  $O_2$  and  $O_3$ ), the network correctly outputs numerically negligible values, demonstrating its ability to avoid false positives. Planetary radius, gravity, and surface pressure are recovered with low bias and dispersion-limited scatter. While atmospheric temperature retrievals show absolute errors of approximately 20 K, its narrow intrinsic range depresses the  $R^2$  metric.

Analysis of the Monte Carlo Dropout posteriors reveals that while the fraction of test points inside the predicted interval increases monotonically with  $\sigma$ , the coverage remains consistently below the ideal Gaussian level. This is especially pronounced for temperature, confirming that the model underestimates epistemic variance. A negative correlation between  $N_2$  and  $O_2$  emerges in Modern-era spectra, where the network compensates for additional  $N_2$  by reducing  $O_2$ , thereby preserving the planet’s bulk composition in the absence of strong  $N_2$  absorption features.

Integrated Gradients shed light on the model’s decision-making process. For Modern Earth, the model correctly weights the Fraunhofer A band for  $O_2$ , and the Hartley–Huggins UV band for  $O_3$ . Under Proterozoic conditions, the LUVOR-B retrieval path effectively nullifies the importance of  $O_2/O_3$ , whereas HabEx/SS still assigns some weight to  $O_2$  in the UV. As biosignatures fade, the model’s feature importance tends to “leak” toward correlated absorbers, most prominently an artificial inflation of  $CO_2$ . In the Archean scenario, the Rayleigh-bright UV continuum drives nearly all feature importance; here, HabEx/SS incorrectly attributes some of this signal to  $O_2/O_3$  as a result of Rayleigh scattering bleeding across adjacent wavelengths.

Credibility curves help to quantify the detection horizons. A 1.5%  $O_2$  mixing ratio is recoverable around F/G-type hosts out to 12 pc, beyond which photometric noise, rather than model bias, becomes the limiting factor.  $O_3$  proves far more robust: its credibility remains above 0.85 across the entire log-abundance range we explored (down to  $-9$ ) for all stellar types and distances, indicating that its detection floor is set by instrumental sensitivity, not by the retrieval algorithm itself.

Our study’s main limitations stem from the simplifications made in the training set. We assumed a vertically uniform atmospheric composition and a complete absence of clouds or hazes. While these assumptions greatly reduce the computational burden of radiative transfer modeling, they compromise physical realism. Furthermore, our model tends to underestimate uncertainties, an issue most ap-



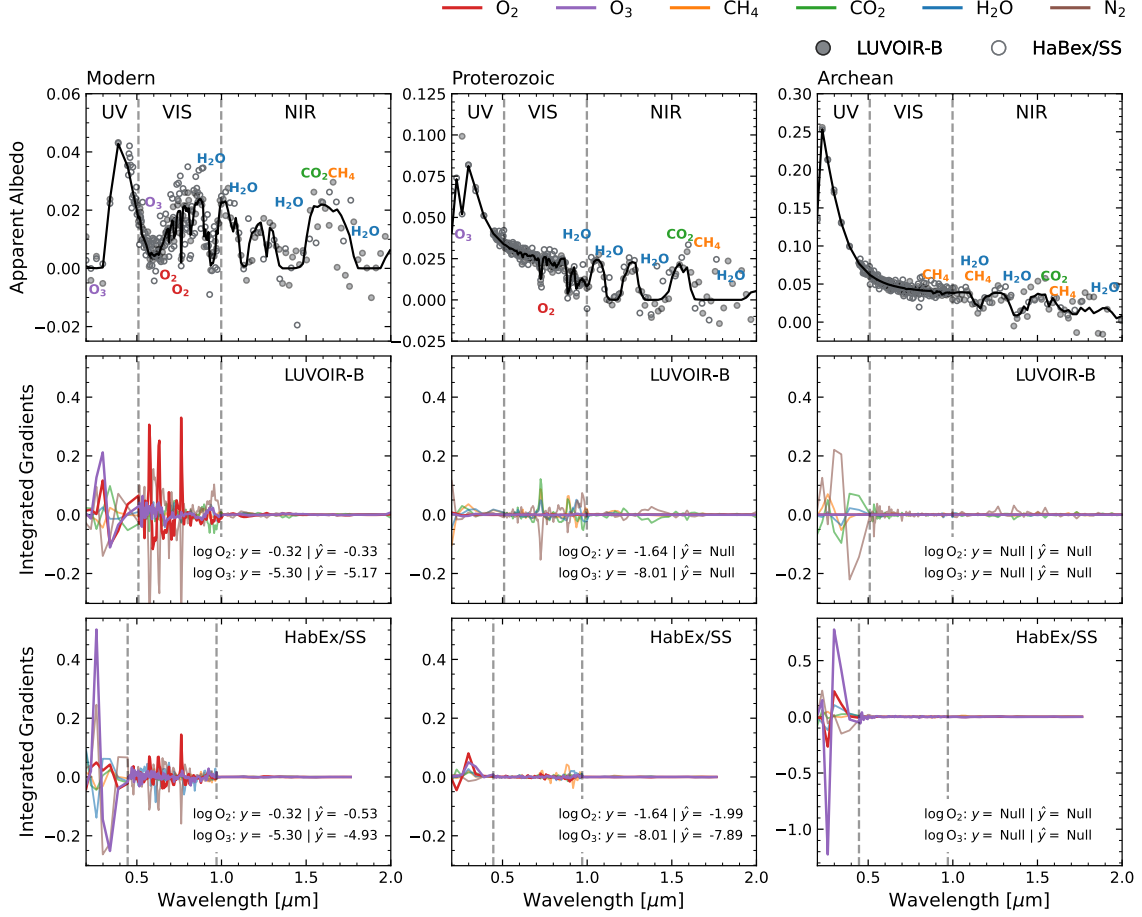


**Figure 7.** Side-by-side comparison of IG attributions for simulated LUVOIR-B (middle row) and HabEx/SS (bottom row) observations of random Modern-Earth, Proterozoic, and Archean samples from the test set. The IG attributions quantify the influence of each spectral bin on the CNN’s prediction for the mixing ratio of each atmospheric gas. The top row shows the corresponding apparent albedo spectra, with  $A(\lambda)$  as a solid black line and  $A_{\text{noisy}}(\lambda)$  as filled gray dots for LUVOIR-B and open circles for HabEx/SS. Key biosignatures,  $\text{O}_2$  (thick red line) and  $\text{O}_3$  (thick violet line), are highlighted against other species (thin lines). Dashed vertical lines mark the instrument’s UV-VIS and VIS-NIR channel boundaries. True or predicted mixing ratios that are exactly zero are labeled “Null” to avoid ambiguity with non-zero values where the logarithm is zero.

parent with atmospheric temperature, whose narrow dynamic range inflates the denominator of the  $R^2$  score and masks reasonable absolute errors of  $\sim 20$  K. These limitations do not invalidate our approach; instead, they clearly map out the necessary improvements for the next generation of synthetic datasets.

Future work must incorporate vertical atmospheric gradients and the effects of multiple scattering by clouds and hazes. It is also essential to extend the spectral domain to the full range of the HWO once its final design is confirmed. Meeting these goals will elevate the CNN from proof of concept to a mission-ready retrieval engine capable of processing direct-imaging spectra with HWO on an operational cadence.

## ACKNOWLEDGEMENTS

We gratefully acknowledge the financial support from the Brazilian agency CAPES (grant No. 88887.622098/2021-00), as well as the STELLAR TEAM at the Federal University of Ceará for our discussions and collaborative support. Part of the research was carried out at the Jet Propulsion Laboratory, California Institute of Technology, under a contract with the National Aeronautics and Space Adminis-

tration (80NM0018D0004). We also extend our thanks to Lorenzo Mugnai for a fruitful discussion, Geronimo Villanueva for his assistance with setting up the PSG, and to Yui Kawashima for providing data on the Proterozoic Earth.

## DATA AVAILABILITY

The trained CNN models for both the HabEx/SS and LUVOIR-B configurations, as well as the corresponding training, validation, and test datasets, have been deposited on Zenodo (DOI: 10.5281/zenodo.15648637).

## REFERENCES

- Abadi M., et al., 2015, TensorFlow: Large-Scale Machine Learning on Heterogeneous Systems, <https://www.tensorflow.org/>
- Ardévol Martínez F., Min M., Kamp I., Palmer P. I., 2022, *A&A*, **662**, A108
- Arney G., et al., 2016, *Astrobiology*, **16**, 873
- Aubin M., et al., 2023, *arXiv e-prints*, p. [arXiv:2309.09337](https://arxiv.org/abs/2309.09337)
- Barclay T., et al., 2013, *Nature*, **494**, 452

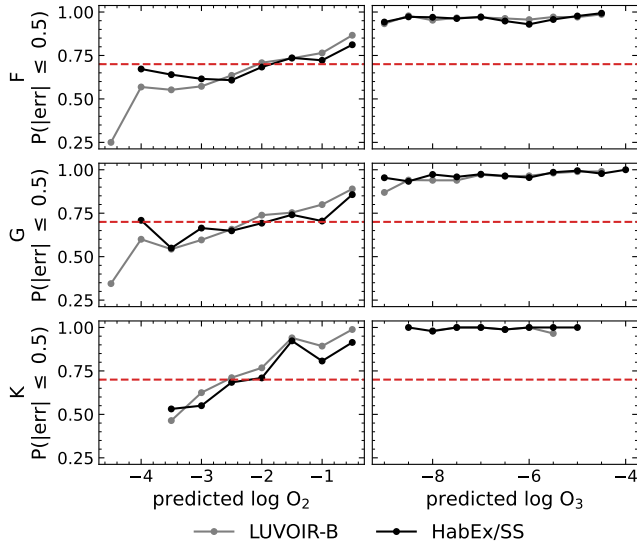


**Figure 8.** Credibility of CNN predictions as a function of the predicted abundance, stratified by host-star spectral class. Each row corresponds to F-, G- and K-type star, while the left and right columns track O<sub>2</sub> and O<sub>3</sub>, respectively. Gray curves refer to LUV0IR-B spectra, black curves to HabEx/SS. The red dashed line marks the credibility threshold  $1 - \delta = 0.7$ .

Bishop C. M., 2006, *Pattern Recognition and Machine Learning* (Information Science and Statistics). Springer-Verlag, Berlin, Heidelberg

Brack A., 1993, *Origins of Life and Evolution of the Biosphere*, 23, 3

Brogi M., Snellen I. A. G., de Kok R. J., Albrecht S., Birkby J., de Mooij E. J. W., 2012, *Nature*, 486, 502

Catling D. C., Kasting J. F., 2017, *Atmospheric Evolution on Inhabited and Lifeless Worlds*. Cambridge University Press

Catling D. C., Zahnle K. J., 2020, *Science Advances*, 6, eaax1420

Changeat Q., Yip K. H., 2023, *RAS Techniques and Instruments*, 2, 45

Charbonneau D., Brown T. M., Noyes R. W., Gilliland R. L., 2002, *ApJ*, 568, 377

Charbonneau D., et al., 2005, *ApJ*, 626, 523

Charbonneau D., et al., 2009, *Nature*, 462, 891

Checlair J. H., et al., 2021, *AJ*, 161, 150

Chen J., Kipping D., 2017, *ApJ*, 834, 17

Choi K., Yi J., Park C., Yoon S., 2021, *IEEE Access*, 9, 120043

Cockell C. S., et al., 2016, *Astrobiology*, 16, 89

Conde A., Domínguez J., 2018, *Journal of Asia-Pacific Biodiversity*, 11, 161

Coston C., Mamajek E., Gilbert E., 2024, in *American Astronomical Society Meeting Abstracts*. p. 259.15

Cuntz M., Guinan E. F., 2016, *ApJ*, 827, 79

Currie M. H., Meadows V. S., Rasmussen K. C., 2023, *Planetary Science Journal*, 4, 83

Damiano M., Hu R., 2022, *AJ*, 163, 299

Damiano M., Hu R., Mennesson B., 2023, *AJ*, 166, 157

Dawson R. I., Johnson J. A., 2018, *ARA&A*, 56, 175

Del Genio A. D., et al., 2019, *ApJ*, 884, 75

Deming L. D., Seager S., 2017, *Journal of Geophysical Research (Planets)*, 122, 53

Estrela R., Swain M. R., Roudier G. M., 2022, *ApJ*, 941, L5

Fortney J. J., Dawson R. I., Komacek T. D., 2021, *Journal of Geophysical Research (Planets)*, 126, e06629

Gal Y., Ghahramani Z., 2015, *arXiv e-prints*, p. arXiv:1506.02142

Gaudi B. S., et al., 2020, *arXiv e-prints*, p. arXiv:2001.06683

Gelaro R., et al., 2017, *Journal of Climate*, 30, 5419

Géron A., 2022, *Hands-on machine learning with Scikit-Learn, Keras, and TensorFlow: Concepts, tools, and techniques to build intelligent systems*. O'Reilly Media, Incorporated

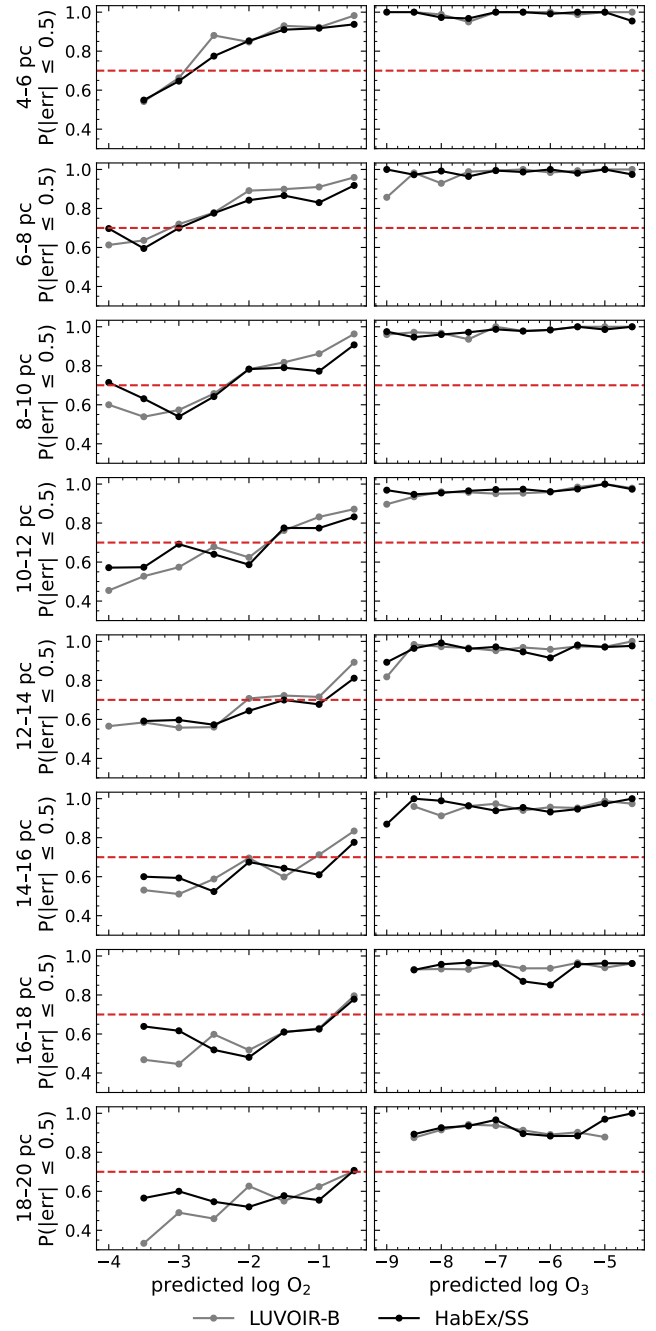


**Figure 9.** Same credibility analysis as Fig. 8, now sliced by distance for FGK stars. Rows are in 2 pc steps, from 4-6 pc (top) to 18-20 pc (bottom).

Gibson N. P., et al., 2010, *MNRAS*, 404, L114

Goyal J. M., et al., 2018, *MNRAS*, 474, 5158

Haghighipour N., 2013, *Annual Review of Earth and Planetary Sciences*, 41, 469

Hatzes A. P., Rauer H., 2015, *ApJ*, 810, L25

Howard A. W., et al., 2013, *Nature*, 503, 381

JWST Transiting Exoplanet Community Early Release Science Team et al., 2023, *Nature*, 614, 649

Kaltenegger L., 2017, *ARA&A*, 55, 433

Kane S. R., 2021, *Planetary Habitability*. IOP Publishing, doi:10.1088/2514-3433/ac2aa1

- Kasting J. F., Whitmire D. P., Reynolds R. T., 1993, *Icarus*, **101**, 108
- Kawashima Y., Rugheimer S., 2019, *AJ*, **157**, 213
- Keles E., Grenfell J. L., Godolt M., Stracke B., Rauer H., 2018, *Astrobiology*, **18**, 116
- Kofman V., Villanueva G., Fauchez T., Mandell A., Johnson T., Payne A., Latouf N., Kelkar S., 2024, arXiv e-prints, p. [arXiv:2411.12708](https://arxiv.org/abs/2411.12708)
- Kopparapu R. K., et al., 2013, *ApJ*, **765**, 131
- Kopparapu R. K., Ramirez R. M., SchottelKotte J., Kasting J. F., Domagal-Goldman S., Eymet V., 2014, *ApJ*, **787**, L29
- Kreidberg L., et al., 2014, *ApJ*, **793**, L27
- Lavie B., et al., 2017, *AJ*, **154**, 91
- LeCun Y., Boser B., Denker J. S., Henderson D., Howard R. E., Hubbard W., Jackel L. D., 1989, *Neural Computation*, **1**, 541
- Legendre P., Gallagher E. D., 2001, *Oecologia*, **129**, 271
- Li S., Song W., Fang L., Chen Y., Ghamisi P., Benediktsson J. A., 2019, *IEEE Transactions on Geoscience and Remote Sensing*, **57**, 6690
- Lyons T. W., Reinhard C. T., Planavsky N. J., 2014, *Nature*, **506**, 307
- Madhusudhan N., Seager S., 2009, *ApJ*, **707**, 24
- Malik A., Moster B. P., Obermeier C., 2022, *MNRAS*, **513**, 5505
- Mamajek E. E., 2019, A Modern Mean Dwarf Stellar Colour and Effective Temperature Sequence, [https://www.pas.rochester.edu/~emamajek/EEM\\_dwarf\\_UBVIJHK\\_colors\\_Teff.dat](https://www.pas.rochester.edu/~emamajek/EEM_dwarf_UBVIJHK_colors_Teff.dat)
- Marshall C. R., 2006, *Annual Review of Earth and Planetary Sciences*, **34**, 355
- Mayor M., Queloz D., 1995, *Nature*, **378**, 355
- McIntyre S. R. N., King P. L., Mills F. P., 2023, *MNRAS*, **519**, 6210
- Morbidelli A., Raymond S. N., 2016, *Journal of Geophysical Research (Planets)*, **121**, 1962
- Müller S., Baron J., Helled R., Bouchy F., Parc L., 2024, *A&A*, **686**, A296
- National Academies of Sciences and Medicine, Engineering 2021, Pathways to Discovery in Astronomy and Astrophysics for the 2020s. The National Academies Press, Washington, DC, doi:10.17226/26141
- Nixon M. C., Madhusudhan N., 2020, *MNRAS*, **496**, 269
- O'Malley T., Bursztein E., Long J., Chollet F., Jin H., Invernizzi L., et al., 2019, KerasTuner, <https://github.com/keras-team/keras-tuner>
- Otegi J. F., Dorn C., Helled R., Bouchy F., Haldemann J., Alibert Y., 2020, *A&A*, **640**, A135
- Owen T., 1980, in Papagiannis M. D., ed., *Astrophysics and Space Science Library Vol. 83, Strategies for the Search for Life in the Universe*. p. 177, doi:10.1007/978-94-009-9115-6\_17
- Pathmaperuma M. H., Rahulamathavan Y., Dogan S., Kondo A. M., 2022, *Sensors*, **22**, 7643
- Pedregosa F., et al., 2011, *Journal of Machine Learning Research*, **12**, 2825
- Phillips M. W., et al., 2020, *A&A*, **637**, A38
- Planavsky N. J., et al., 2014, *Nature Geoscience*, **7**, 283
- Robinson T. D., Salvador A., 2023, *Planetary Science Journal*, **4**, 10
- Robinson T. D., Fortney J. J., Hubbard W. B., 2017, *ApJ*, **850**, 128
- Rugheimer S., Kaltenegger L., 2018, *ApJ*, **854**, 19
- Rumelhart D. E., Hinton G. E., Williams R. J., 1985, Technical report, Learning Internal Representations by Error Propagation. Institute for Cognitive Science, University of California, San Diego
- Schwieterman E. W., et al., 2018, *Astrobiology*, **18**, 663
- Seager S., 2010, *Exoplanet Atmospheres: Physical Processes*. Princeton University Press
- Seager S., 2013, *Science*, **340**, 577
- Shallue C. J., Vanderburg A., 2018, *AJ*, **155**, 94
- Sundararajan M., Taly A., Yan Q., 2017, arXiv e-prints, p. [arXiv:1703.01365](https://arxiv.org/abs/1703.01365)
- The LUVVOIR Team 2019, arXiv e-prints, p. [arXiv:1912.06219](https://arxiv.org/abs/1912.06219)
- Tompson J., Goroshin R., Jain A., LeCun Y., Bregler C., 2014, arXiv e-prints, p. [arXiv:1411.4280](https://arxiv.org/abs/1411.4280)
- Tsiaras A., Waldmann I. P., Tinetti G., Tennyson J., Yurchenko S. N., 2019, *Nature Astronomy*, **3**, 1086
- Valizadegan H., et al., 2022, *ApJ*, **926**, 120
- Villanueva G. L., Smith M. D., Protopapa S., Faggi S., Mandell A. M., 2018, *J. Quant. Spectrosc. Radiative Transfer*, **217**, 86
- Villanueva G. L., Liuzzi G., Faggi S., Protopapa S., Kofman V., Fauchez T., Stone S. W., Mandell A. M., 2022, Fundamentals of the Planetary Spectrum Generator. NASA Goddard Space Flight Center
- Waldmann I. P., 2016, *ApJ*, **820**, 107
- Waldmann I. P., Tinetti G., Rocchetto M., Barton E. J., Yurchenko S. N., Tennyson J., 2015, *ApJ*, **802**, 107
- Way M. J., et al., 2017, *ApJS*, **231**, 12
- Yadav D., Kapoor K., Yadav A. K., Kumar M., Jain A., Morato J., 2024, *Earth Science Informatics*,
- Yip K. H., Changeat Q., Nikolaou N., Morvan M., Edwards B., Waldmann I. P., Tinetti G., 2021, *ApJ*, **162**, 195
- Yip K. H., Changeat Q., Al-Refaie A., Waldmann I. P., 2024, *ApJ*, **961**, 30
- Zahnle K., 1998, in Woodward C. E., Shull J. M., Thronson Harley A. J., eds, *Astronomical Society of the Pacific Conference Series Vol. 148, Origins*. p. 364
- Zahnle K. J., Catling D. C., 2013, in 44th Annual Lunar and Planetary Science Conference. Lunar and Planetary Science Conference. p. 2787
- Zahnle K. J., Catling D. C., 2017, *ApJ*, **843**, 122
- Zamanzadeh Darban Z., Webb G. I., Pan S., Aggarwal C. C., Salehi M., 2022, arXiv e-prints, p. [arXiv:2211.05244](https://arxiv.org/abs/2211.05244)
- Zhang J., Xia Y., Wu Q., Xie Y., 2017, arXiv e-prints, p. [arXiv:1706.09092](https://arxiv.org/abs/1706.09092)
- Zhang M., Chachan Y., Kempton E. M. R., Knutson H. A., 2019, *PASP*, **131**, 034501
- Zingales T., Waldmann I. P., 2018, *AJ*, **156**, 268
- Zorzan S., et al., 2025, *The Astrophysical Journal Supplement Series*, **277**, 38

## APPENDIX A: COMPLEMENTARY FIGURES

This paper has been typeset from a  $\text{\LaTeX}$  file prepared by the author.

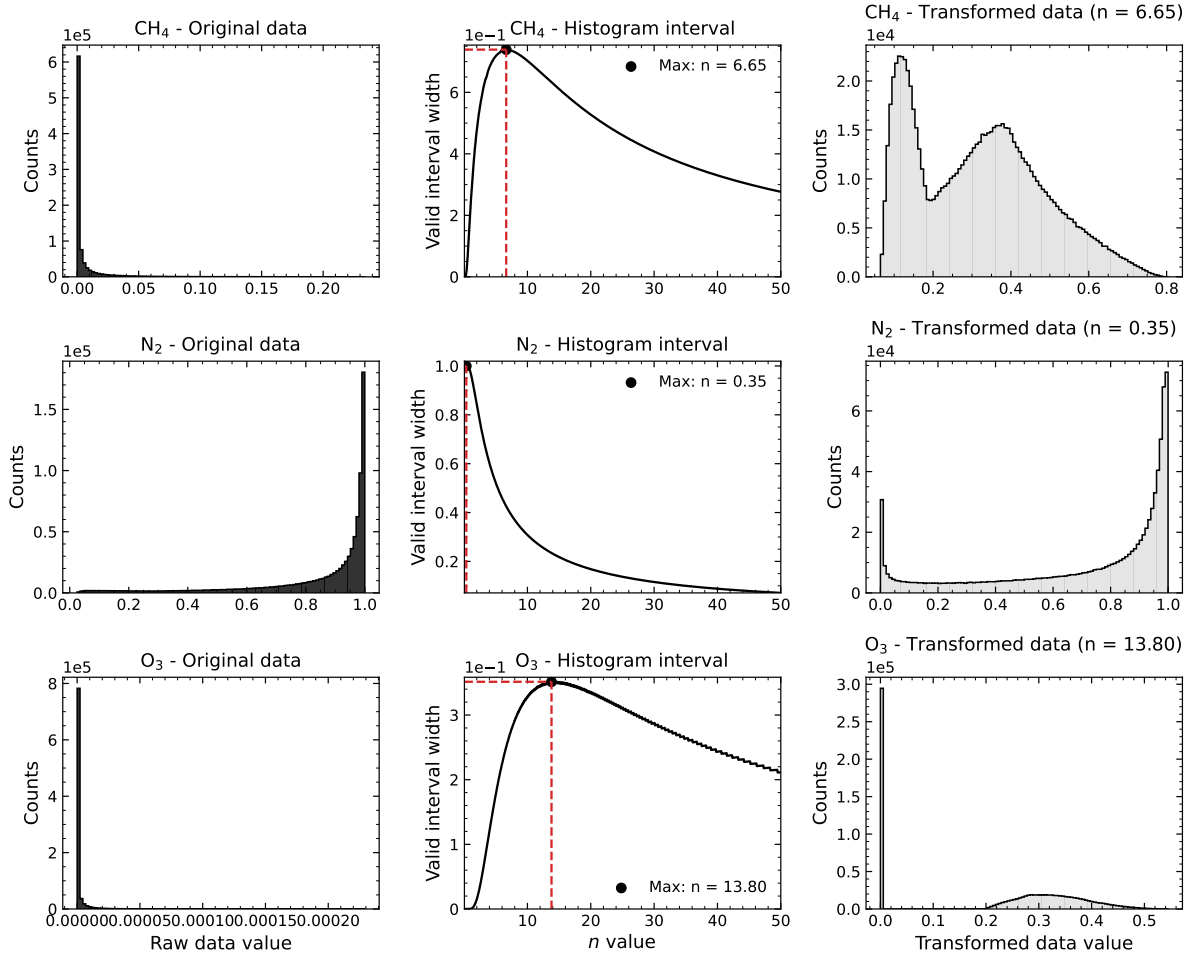


**Figure A1.** Examples of species distributions. The left column shows the original distribution of the data. The middle column shows  $\vartheta_1(n_i)$  and the best  $n_i$  indicated. The right column shows the new distribution of each species after the transformation in Equation 19 is applied with the best  $n_i$ .



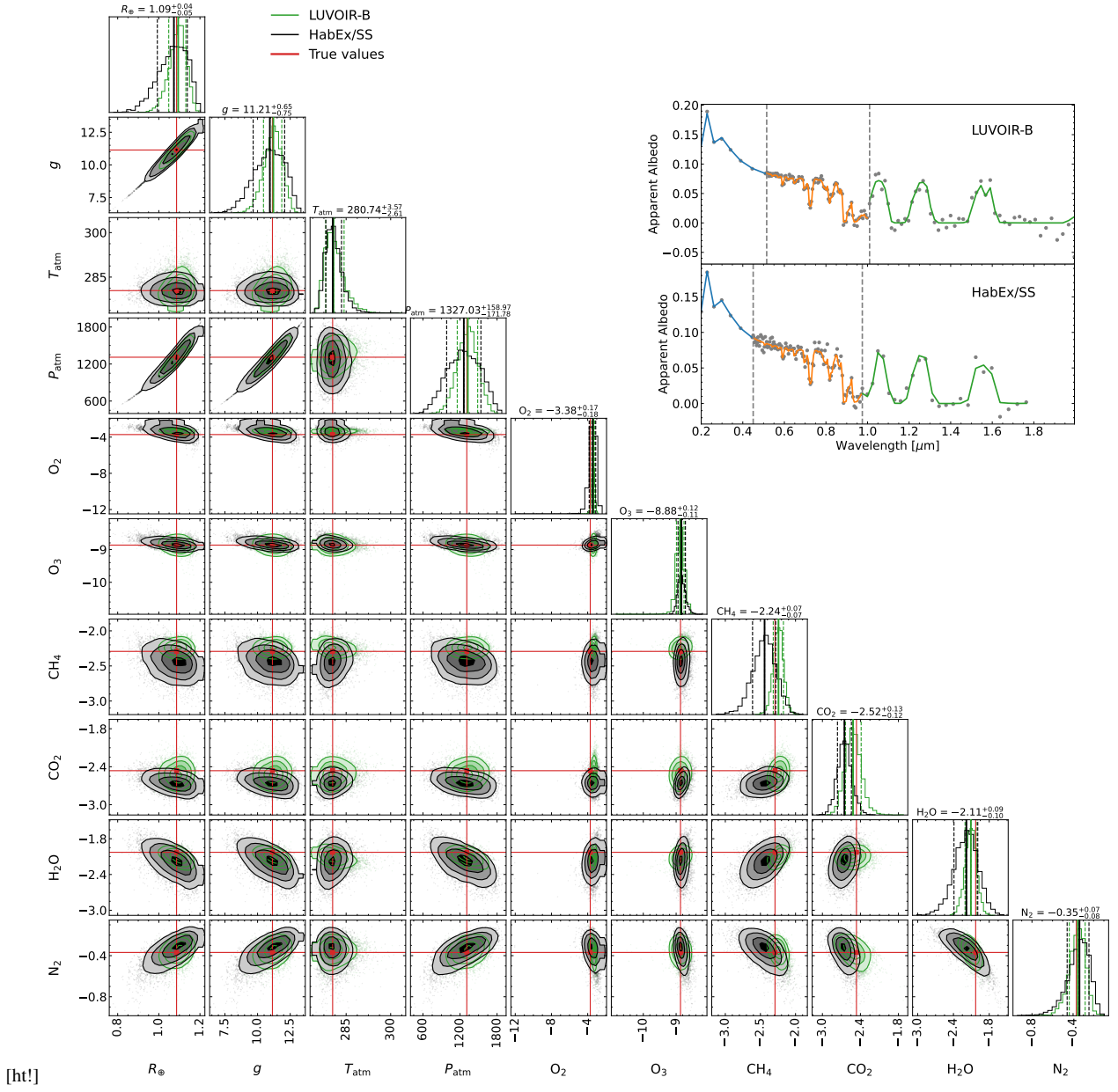
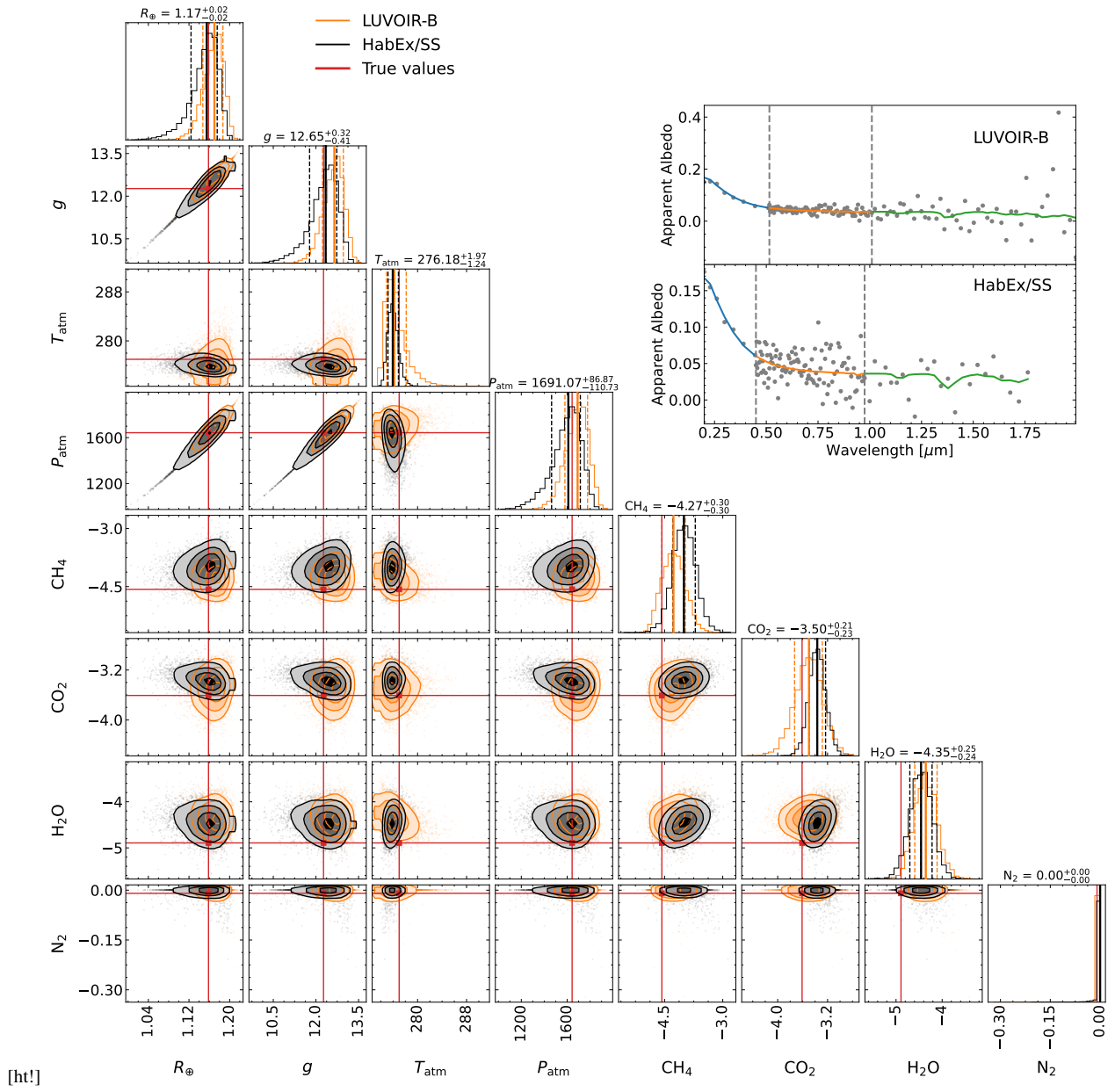
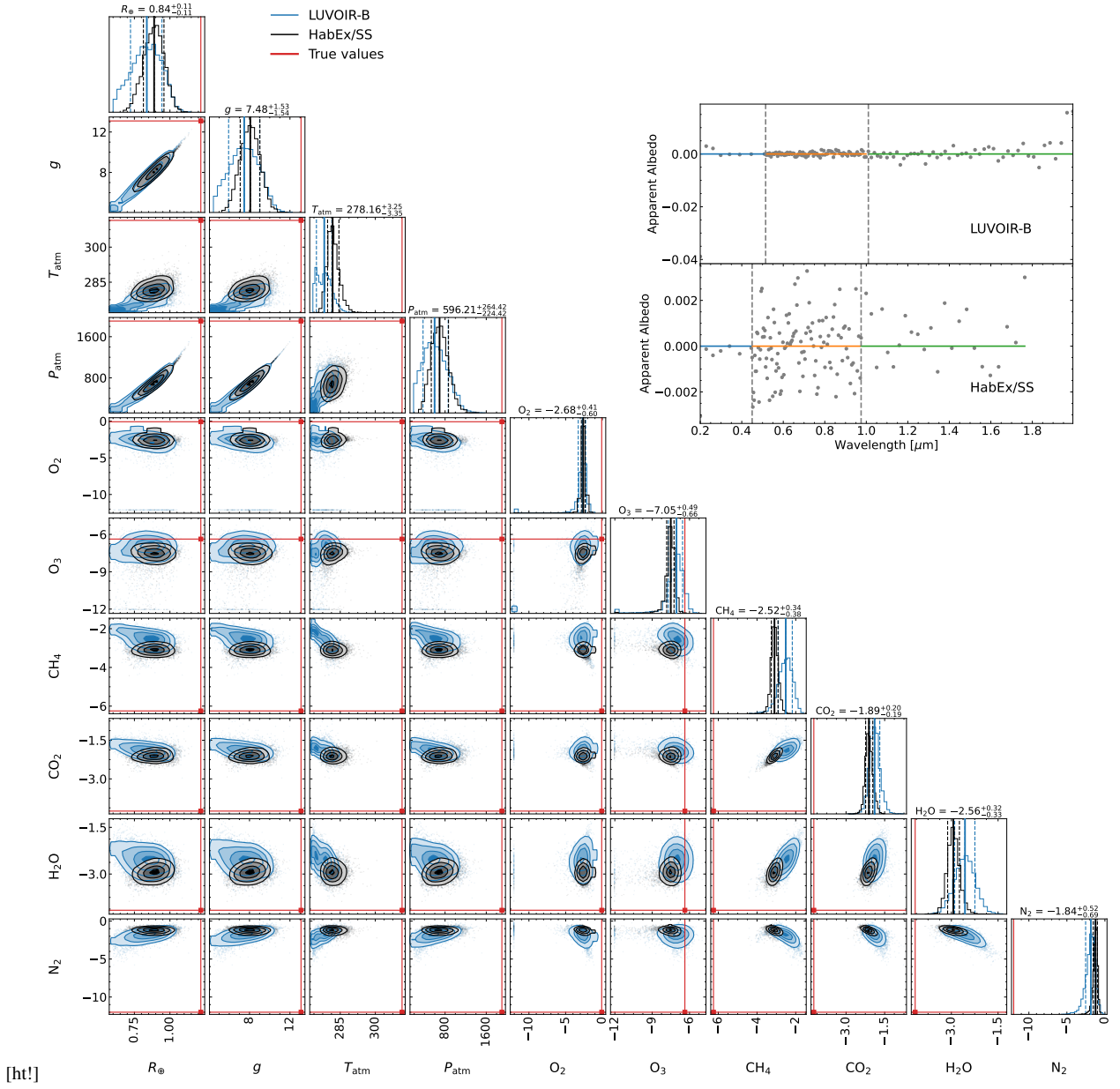


Figure A2. Same as Fig. 5, but for the best Proterozoic Earth sample in the test set.



**Figure A3.** Same as Fig. 5, but for the best Archean Earth sample in the test set.



**Figure A4.** Same as Fig. 5, but showing the worst case in the Modern test set. Here, the true parameter vector lies furthest from the predictive means of both models.